1 **Title: Genome instability drives epistatic adaptation in the human pathogen *Leishmania***

2 **Authors:** Giovanni Bussotti[1,2], Laura Piel[2,a], Pascale Pescher[2], Malgorzata A. Domagalska[3], K.

3 Shanmugha Rajan[4], Smadar Cohen-Chalamish[4], Tirza Doniger[4], Disha-Gajanan Hiregange[5],

4 Peter J Myler[6-10], Ron Unger[4], Shulamit Michaeli[4], and Gerald F. Späth[2,*]

5 **Affiliations:**

6 [1]Institut Pasteur – Bioinformatics and Biostatistics Hub – C3BI, USR 3756 IP CNRS – Paris,

7 France.

8 [2]Institut Pasteur, INSERM U1201, Unité de Parasitologie moléculaire et Signalisation, Paris,

9 France.

10 [3]Institute of Tropical Medicine, Molecular Parasitology Unit, B-2000, Antwerp, Belgium.

11 [4]The Mina and Everard Goodman Faculty of Life Sciences and Advanced Materials and

12 Nanotechnology Institute, Bar-Ilan University, Ramat-Gan 52900, Israel.

13 [5] Department of Chemical and Structural Biology, Weizmann Institute of Science, Rehovot,

14 7610001 Israel.

15 [6] Seattle Structural Genomics Center for Infectious Disease, Seattle, Washington, USA.

16 [7] Department of Biomedical Informatics and Medical Education, University of Washington,

17 Seattle, Washington, USA.

18 [8] Department of Pediatrics, University of Washington, Seattle, Washington, USA.

19 [9] Department of Global Health, University of Washington, Seattle, Washington, USA.

20 [10] Center for Global Infectious Disease Research, Seattle Children's Research Institute, Seattle,

21 Washington, USA peter.myler@seattlechildrens.org.

[a] Current address: Current address: Institut de Biologie Intégrative de la Cellule (I2BC) UMR 9198, Gif-sur-Yvette, France.

*corresponding author: Gerald Spaeth, Gerald.spaeth@pasteur.fr

Abstract. How genome instability is harnessed for fitness gain despite its potential deleterious effects is largely elusive. An ideal system to address this important open question is provided by the protozoan pathogen *Leishmania*, which exploits frequent variations in chromosome and gene copy number to regulate expression levels. Using ecological genomics and experimental evolution approaches we provide first evidence that *Leishmania* adaptation relies on epistatic interactions between functionally associated gene copy number variations in pathways driving fitness gain in a given environment. We further uncover post-transcriptional regulation as a key mechanism that compensates for deleterious gene dosage effects and provides phenotypic robustness to genetically heterogenous parasite populations. Finally, we correlate dynamic variations in snoRNA gene dosage with changes in rRNA 2'-*O*-methylation and pseudouridylation, suggesting translational control is an additional layer of parasite adaptation. *Leishmania* genome instability is thus harnessed for fitness gain by genome-dependent variations in gene expression, and genome-independent, compensatory mechanisms. This allows for polyclonal adaptation and maintenance of genetic heterogeneity despite strong selective pressure. The epistatic adaptation described here needs to be considered in *Leishmania* epidemiology and biomarker discovery, and may be relevant to other fast evolving, eukaryotic cells that exploit genome instability for adaptation, such as fungal pathogens or cancer.

One Sentence Summary:

Epistatic interactions harness genome instability for *Leishmania* fitness gain.

Main Text:

Darwinian evolution plays a central, yet poorly understood, role in human disease. Iterative rounds of genetic mutation and environmental selection drive tumor development, microbial fitness and therapeutic failure. Genome instability is a key source for genetic and phenotypic diversity, often defining disease outcome (*1-4*). However, the mechanism(s) by which genome instability is harnessed for fitness gain despite its potential deleterious effects remain largely elusive. Here we investigate this question in the protozoan parasite *Leishmania*, which causes devastating human infections. These parasite cycle between insect-stage promastigotes that infected *Phlebotomus* sand flies, and intracellular amastigotes that proliferate inside phagolysosomes of mammalian macrophages. Genome instability is hallmark of *Leishmania* biology, since these parasites lack promoter-dependent gene regulation (*5, 6*), but exploit chromosome and gene copy number variations to regulate mRNA abundance by gene dosage (*7-11*). In the absence of confounding transcriptional control, *Leishmania* thus represents an ideal system to investigate the role of genome instability in fast-evolving eukaryotic cells.

Here we uncover complex epistatic interactions between gene copy number variations and compensatory, transcriptomic responses as key processes that harness genome instability for fitness gain in *Leishmania*. Our data may be broadly applicable to pathogenic fungi or cancer cells, known to exploit genome instability for adaptation.

67 **Results**

68 ***Leishmania* genomic adaptation is governed by epistatic interactions between gene copy**
69 **number variations.** We first assessed the level of copy number variation across 204 *Leishmania*
70 *donovani* clinical isolates from the Indian sub-continent (ISC) (*12*). This collection includes a core
71 group of 191 strains that are genetically highly homogenous as judged by the small number of
72 single nucleotide variants (SNVs) (<2,500 total), which provided us with a useful benchmark to
73 study the dynamics of copy number variations (CNVs) across a large number of quasi-clonal
74 populations. DNA read depth analysis of these isolates revealed important CNVs in both coding
75 and non-coding regions, with amplifications and deletions affecting respectively 14% and 4% of
76 the genome (**Fig. 1A-B, Tables S1-S2**). Analysing the statistical association of observed CNVs
77 with repetitive sequence elements uncovered 10 novel DNA repeats that could drive *Leishmania*
78 genome instability through microhomology-mediated, break-induced replication as observed for
79 human CNVs (*13*) (**Fig. 1C**, **Fig. S1, Table S3**). Gene dosage changes were not random but clearly
80 under selection as judged by the reproducibility of genetic interactions across independent isolates
81 and the enrichment of amplified genes in biological functions associated with fitness gain.
82 Statistically significant interactions were observed between positive (correlating) and negative
83 (anti-correlating) read depth variations (**Fig. 1D**, **Fig. S2-S3**, **Table S4-S5**), including a highly
84 connected Network Cluster (NC) containing 60 co-amplified tRNA genes encoded on 16 different
85 chromosomes (NC1, **Fig. 1D**, **Fig. S4**, **Tables S6-S7**). Natural selection of gene CNVs is further
86 supported by (i) their independent emergence across phylogenetically distinct strains providing
87 evidence for evolutionary convergence, (ii) the very high copy number observed for certain genes
88 (up to 30-fold) suggesting strong, positive selection, and (iii) the global enrichment of read depth
89 variations in phenotypically silent, intergenic regions, suggesting purifying selection against

90 deleterious effects caused by gene CNVs (**Fig. 1E-G**, **Fig. S5, Table S8-S10**). Together our data
91 provide the first evidence that *Leishmania* genomic adaptation is governed by gene CNVs through
92 highly dynamic, functional interactions that are under natural selection. These interactions define
93 a novel form of epistasis at the gene (rather than nucleotide) level, with the phenotypic effect of a
94 given gene amplification being dependent on co-amplification of functionally related genes.
95
96 **Epistatic adaptation drives polyclonal fitness gain *in vitro*.** We next used an experimental
97 evolution approach to directly assess the link between epistatic interactions and fitness gain in
98 hamster-derived *L. donovani* parasites during adaptation to *in vitro* culture (*10*). Following
99 normalization for karyotypic variations (**Fig. S6A, Table S11**), changes in read depth were
100 monitored between passages 2 (P2, two weeks in culture) and 135 (P135, 36 weeks in culture),
101 corresponding to approximately 20 and 3,800 generations. Our analysis revealed co-amplification
102 of coding and non-coding (nc) genes and gene clusters that are functionally linked to fitness gain
103 in culture (*i.e.* accelerated cell proliferation), including genes encoding for rRNAs, tRNAs,
104 snRNAs, snoRNAs, SLRNAs, and ribosomal proteins (**Fig. 2A**, **Fig. S6B** and **Tables S12-S14**).
105 Epistatic adaptation thus increases translation efficiency, thus overcoming the major rate limiting
106 steps for fast growing populations (*14*). This functional link between a given fitness phenotype
107 and its underlying epistatic network opens unexplored venues for the discovery of *Leishmania*
108 biomarkers, which may be represented by complex genetic interactions rather than individual loci.
109
110 Unexpectedly, as well as gene amplification, we discovered that gene depletion is also a
111 major driver for environmental adaptation and fitness gain. We identified a genomic deletion of
112 11 kb containing a single gene encoding for a NIMA-related kinase gene (Ld1S_360735700),

113 which is gradually selected in the adapting promastigote population from a pre-existing mutant
114 that was detected in splenic amastigotes (**Fig. 2B**, **Fig. S7A** and **B**). Clonal analysis of the P20
115 population revealed the presence of the spontaneous knockout (spo-KO) in six out of eight
116 individual clones (**Fig. 2C**). These spo-KO clones were clearly not the descendants of a single
117 founder cell but were of independent, polyclonal origin as judged by their distinct gene CNV
118 profiles (**Fig. 2C**, **Table S15**), and their polyphyletic clustering based on SNVs compared to wild-
119 type (WT) clones (**Fig. 2D, Table S16**). This evolutionary convergence strongly supports natural
120 selection of the deletion during culture adaptation and suggests a potential role of the deleted
121 NIMA kinase in growth restriction, which we further assessed by gene editing.
122
123 **Toxic gene dosage effects are compensated at post-transcriptional levels.** Unlike the spo-KO
124 clones, CRISPR/Cas9-generated, NIMA knock out mutants (cri-KO) (**Fig. S7C** and **D**) were not
125 viable, while heterozygous mutants showed a strong growth defect, which was partially rescued
126 by episomal over-expression of the NIMA kinase gene (**Fig. 3A**). This paradoxical result suggests
127 that spo-KO cells must have evolved mechanisms that can compensate for the loss of this essential
128 gene. Read depth analyses of the spo-KO and WT clones ruled out genetic compensation (**Table**
129 **S15**). In contrast, RNAseq analysis revealed highly reproducible, compensatory transcript profiles
130 in the six independent spo-KO clones (**Fig. 3B**, **Table S17**). Our analysis revealed reduced stability
131 in spo-KO clones of 23 transcripts implicated in flagellar biogenesis (**Fig. S8**), which correlated
132 with reduced motility (data not shown). Loss of motility may represent a fitness trade-off,
133 providing energy required for accelerated *in vitro* growth. On the other hand, we identified 350
134 transcripts with increased abundance (Table S17, second sheet), which either result from increased
135 gene dosage or mRNA post-transcriptional stabilization. Direct comparison of DNA and RNA

136 reads depth variations allowed us to distinguish between these two possibilities and identified a
137 set of transcripts whose expression changes between WT and spo-KO did not correlate with gene
138 dosage. In absence of transcriptional regulation in *Leishmania* (*5*), the abundance of these
139 transcripts is likely regulated by differential mRNA turn-over. Increased abundance was observed
140 in spo-KO clones for the mRNA of another NIMA-related kinase (Ld1S_360735800) encoded
141 adjacent to the deleted region, suggesting a direct, post-transcriptional compensation of kinase
142 functions (**Fig. 3C, Table S18**). Likewise, we observed increased stability for functionally related
143 small, non-coding RNAs, including 43 snoRNAs, and various rRNAs and tRNAs (**Fig. 3D, Table**
144 **S18**), suggesting ribosomal biogenesis and translational regulation as yet another level of non-
145 genomic adaptation. Together our data identify gene deletion and compensatory, post-
146 transcriptional responses as novel drivers of *Leishmania* fitness gain.
147
148 **The non-coding RNome as a novel driver of *Leishmania* fitness gain.** The selective stabilization
149 of snoRNAs during early culture adaption (P2-P20) suggests these non-coding RNAs are key
150 drivers in *Leishmania* fitness gain. We confirmed this possibility in long-term adapted parasites
151 that were continuously cultured for ~3,800 generations (P135). Read depth analysis revealed
152 selective amplification of snoRNAs, which was confirmed in an independent, long-term
153 evolutionary experiment conducted until passage 125 (P125, **Fig. 4A**, **Fig. S9** and **Table S19**).
154 Surprisingly, rather than amplification of individual snoRNA genes, increased read depth was
155 caused by the recovery of a single locus on chromosome 33 containing a cluster of 15 snoRNA
156 genes in the P135 population, but was depleted in the original amastigote population (**Fig. 4B**).
157 The restoration of this locus between P20 and P135 is further proof that snoRNAs are under
158 positive selection during culture adaptation. Rather than gene amplification, the recovery of this

159 locus is more likely due to the selection of a small sub-population that penetrated the culture
160 between P20 and P135, similar to what we observed for the NIMA kinase spo-KO. The mosaic
161 structure of this locus is further supported by the CNVs we detected in independent amastigotes
162 isolates (**Fig. 4C**, **Fig. S10**). Thus, while short-term adaptation in *Leishmania* is governed by
163 control of RNA stability, long-term adaptation occurs through more cost-efficient gene dosage
164 regulation. Increased snoRNA abundance likely satisfies a quantitative need for ribosomal
165 biogenesis in our fast-growing cultures. However, changes in snoRNA expression can also affect
166 the nature and quality of ribosomes (*15, 16*).

167 In the following we assessed the possibility of such fitness-adapted ribosomes in
168 *Leishmania* especially since snoRNA genes guiding 2'-*O*-methylation (Nm) and pseudouridine
169 (Ψ) modifications were extensively amplified. Amplification of snoRNAs should lead to increased
170 modifications on sites that are accessible for modification. The mapping of Nm via RiboMeth-seq
171 (*17*) revealed an increased level of modification for 18 sites by at least two fold (**Table S20**), while
172 the mapping of pseudouridylation by Ψ-seq (*18, 19*) showed increase for 5 Ψ sites (**Table S21**)
173 during adaptation from P2 to P135. Interestingly, the hyper-modified Nm sites are localized around
174 the peptidyl-transferase centre (PTC) and mRNA entrance tunnel, whereas the hyper-modified Ψ
175 sites are located in the PTC itself (**Fig. 4D-E**, **Fig. S11**). Together, our data reveal a complex model
176 of *Leishmania* fitness gain, where epistatic interactions between gene amplifications and
177 compensatory responses at post-transcriptional levels harnesses *Leishmania* genome instability for
178 polyclonal adaptation (**Figure 4F**).
179
180

181 **Discussion**

182 A common strategy in microbial evolutionary adaptation is known as 'bet-hedging', where the
183 fitness of a population in changing environments is increased by stochastic fluctuations in gene
184 expression that are regulated at epigenetic levels (*20-24*). The protozoan pathogen *Leishmania*
185 largely lacks transcriptional regulation, raising the question on how these parasites generate
186 variability in transcript abundance and phenotype required for adaptation (*5, 6*). Our data uncover
187 an alternative mechanism of bet-hedging that has evolved based on the unique biology of
188 *Leishmania*.

189 First, we provide evidence that *Leishmania* genome instability may be driven by 10 new
190 repetitive DNA elements associated with genome-wide amplifications and deletions, both of which
191 are under positive and purifying selection. *Leishmania* thus compensates for the absence of
192 stochastic gene regulation by the generation of stochastic gene CNVs, which are known to cause
193 dosage-dependent changes in transcript abundance (*7-11*). Second, we reveal an important role for
194 post-transcriptional regulation in *Leishmania* fitness gain, which (i) compensates for the
195 deleterious deletion of a NIMA kinase by selectively stabilizing the transcripts of an orthologous
196 kinase, (ii) allows for gene dosage-independent increase in the abundance of non-coding RNAs
197 (SLRNAs, snoRNAs) required for proliferation, and (iii) provides phenotypic robustness to
198 genetically heterogenous populations as documented by the converging transcript profiles of
199 independent NIMA spo-KO mutants. This adaptation process guards against toxic gene dosage
200 effects and simultaneously increases the phenotypic landscape available to *Leishmania* for
201 adaptation *via* gene deletions and compensatory transcriptional responses. Significantly, the
202 NIMA orthologue, as well as the SLRNA and snoRNA loci are amplified during long-term culture
203 (**Fig. 4B**, **Fig. S6B**, **Fig. S9**), revealing a two-step adaption process reminiscent to yeast (*25*),

204 implicating a first, post-transcriptional mechanism *via* transient changes in RNA stability,
205 followed by a second, genomic mechanism *via* selection for stable CNVs.

206 The dynamic changes in snoRNA stability and gene copy number observed in our
207 experimental evolution system identifies this class of ncRNAs as an unexpected driver of
208 *Leishmania* fitness gain. snoRNAs guide rRNA modification and processing, as well as
209 modification of snRNAs and additional non-coding ncRNAs (*26, 27*). Changes in snoRNA gene
210 copy number and transcript abundance during parasite adaptation correlated with hyper-
211 modification of rRNAs, known to affect the quality and translation specificity of the ribosome. It
212 is interesting to speculate that these specialized ribosomes represent an additional layer of
213 regulation at translational level that can further counteract toxic gene dosage effects, provide
214 phenotypic robustness and adapt the proteome profile to a given environment, much like it was
215 observed in cancer cells or during differentiation of stem cells (*28, 29*).

216 Our findings have important clinical implications for *Leishmania* infection. *Leishmania*
217 adapts to various environmental cues, notably the presence of anti-leishmanial drugs. In contrast
218 to high frequency amplifications observed during experimental drug treatment in culture (*30-32*),
219 treatment failure and drug resistance observed during natural infection may evolve through multi-
220 locus, epistatic interactions such as those described here, which can balance the fitness trade-off
221 between drug resistance and infectivity (*33*). Therefore, our data define biological networks, rather
222 than individual genes, as novel biomarkers with potential diagnostic or prognostic value.
223 Conceivably, the epistatic mechanisms we uncover in *Leishmania* can be of broader relevance to
224 other human pathologies caused by fast evolving eukaryotic cells exploiting genome instability for
225 polyclonal adaptation, such as cancer cells. While single nucleotide, epistatic interactions are
226 recognized as important drivers of tumor development (*34, 35*), the role of epistatic interactions

227 between structural mutations and between the genome and transcriptome in drug-resistant cancer
228 cells remains to be elucidated (*36*).

229 In conclusion, our results propose a novel model of *Leishmania* fitness gain (**Fig. 4F**),
230 where polyclonal adaptation of mosaic populations is driven by epistatic interactions that (i) buffer
231 the detrimental effects of genome instability, (ii) coordinate expression of functionally related
232 genes, and (iii) generate beneficial phenotypes for adaptation. This mechanism of fitness gain
233 avoids genetic death by maintaining heterogeneity in competing parasite populations under
234 environmental selection and may be generally applicable to other eukaryotic systems that adapt
235 through genome instability.

236

237

Acknowledgments:

Funding: This study was supported by a seeding grant from the Institut Pasteur International Department to the LeiSHield Consortium, the EU H2020 project LeiSHield-MATI - REP-778298-1, the Fondation pour la Recherche Médicale (grant number FDT201805005619), the Flemish Ministry of Science and Innovation (MADLEI, SOFI Grant 754204) and a grant from CAMPUS France and the Israeli Ministry of Science and Technology PHC MAIMONIDE 2018-2019-Projet N° 41131ZD. We thank Cedric Notredame and Jean-Claude Dujardin for critical reading of the manuscript.

Author contributions: Conceptualization, G.B., L.P., P.P., M.A.D., T.D., R.U. S.M. and G.F.S.; Methodology, G.B., L.P., P.P., K.S.R, S.C.C, D.G.H., T.D., R.U. and G.F.S.; Software, G.B., T.D. and R.U.; Formal Analysis, G.B., L.P., P.P. and G.F.S.; Investigation, G.B., L.P., P.P. and G.F.S.; Writing – Original Draft, G.B., L.P., P.P. and G.F.S.; Writing – Review & Editing, G.B., L.P., P.P., M.A.D., T.D., P.J.M, R.U. S.M. and G.F.S.; Supervision, G.F.S., R.U. and S.M.; Funding Acquisition, G.F.S., S.M.

Competing interests: Authors declare no competing interests.

Data and materials availability:

Reads were deposited in the Sequence Read Archive (SRA) database (*37*) and are publicly available under accession no PRJNA605972. All data is available in the main text or the supplementary materials.

259 **Fig. 1**

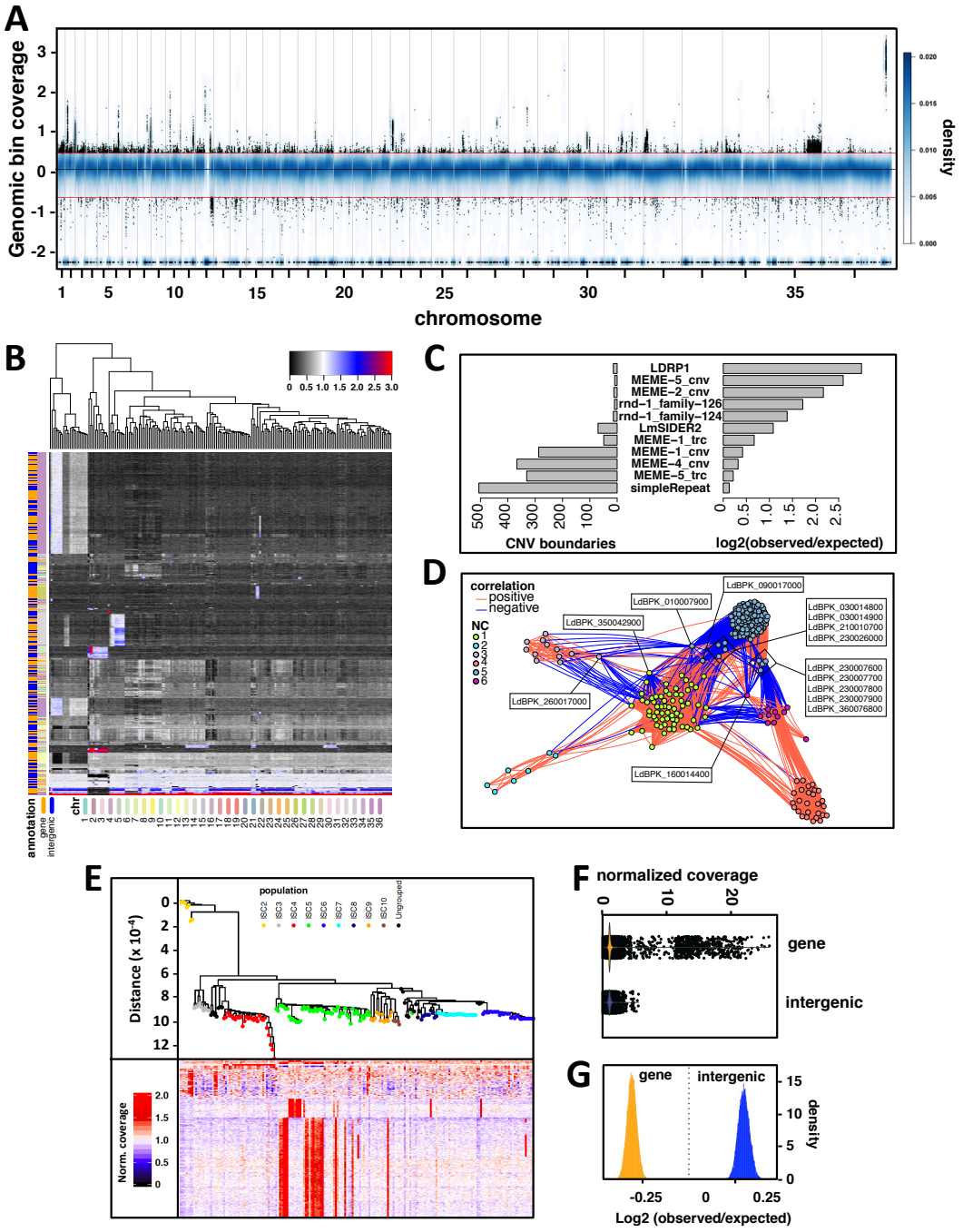

260

261 **Genome-wide mapping of copy number variations (CNVs), their environmental selection,**

262 **and epistatic interactions.** (**A**) Genome-wide normalized coverage values in natural logarithm

263 scale (*y*-axis) across the 36 chromosomes (*x*-axis) for 204 *Leishmania donovani* field isolates from

264 the Indian Sub-continent (*12*). The *x*-axis reports the position of genomic windows along the
265 chromosomes. The smoothed blue color represents the 2D kernel density estimate of genomic bins.
266 A sample of 50,000 genomic bins with normalized coverage ≥ 1.5 or ≤ 0.5 are materialized as
267 black dots. The black horizontal line and the two red lines indicate normalized coverage values of
268 1.5, 1 and 0.5. (**B**) Heatmap generated for the 204 clinical isolates (columns) showing their
269 phylogenetic relationship as a function of CNV bins (rows). The color scale reflects the deviation
270 from the minimum bin coverage observed across all genomes. The presence of annotated genes
271 and the chromosomal location of the CNVs are indicated by the two colored columns on the left.
272 The color code is defined in the legend below the plot. (**C**) Association between CNVs and
273 repetitive elements. The bar plots show the number of observed overlap instances between the
274 boundaries of the CNV regions and repetitive elements (left panel), and the log2 ratio between the
275 observed and expected overlap events over 10,000 randomizations (right panel). (**D**) Gene CNV
276 network analysis. The nodes represent gene CNVs while the edges indicate statistically significant
277 positive (red) and negative (blue) correlations observed in the 204 field isolates. The nodes are
278 colored according to the predicted network clusters (NC). (**E**) Phylogenetic tree based on SNVs
279 (>90% frequency) (upper panel) for the ISC core population comprising 191 isolates (*12*) (not
280 including the distant ISC1 strains (*38*) – for full phylogeny see **Fig. S5**). The heatmap (lower panel)
281 shows the normalized gene sequencing coverage across genomes (rows). To ease the visualization,
282 gene amplifications with normalized coverage > 2 are indicated as 2. (**F**) Violin plot showing the
283 distributions of the normalized genomic coverage values of the collapsed CNV positions (dots)
284 matching genic and intergenic regions. (**G**) Log2 ratio distributions of observed and expected
285 nucleotide overlap between collapsed CNV regions and gene/intergenic annotations.

286 **Fig. 2**

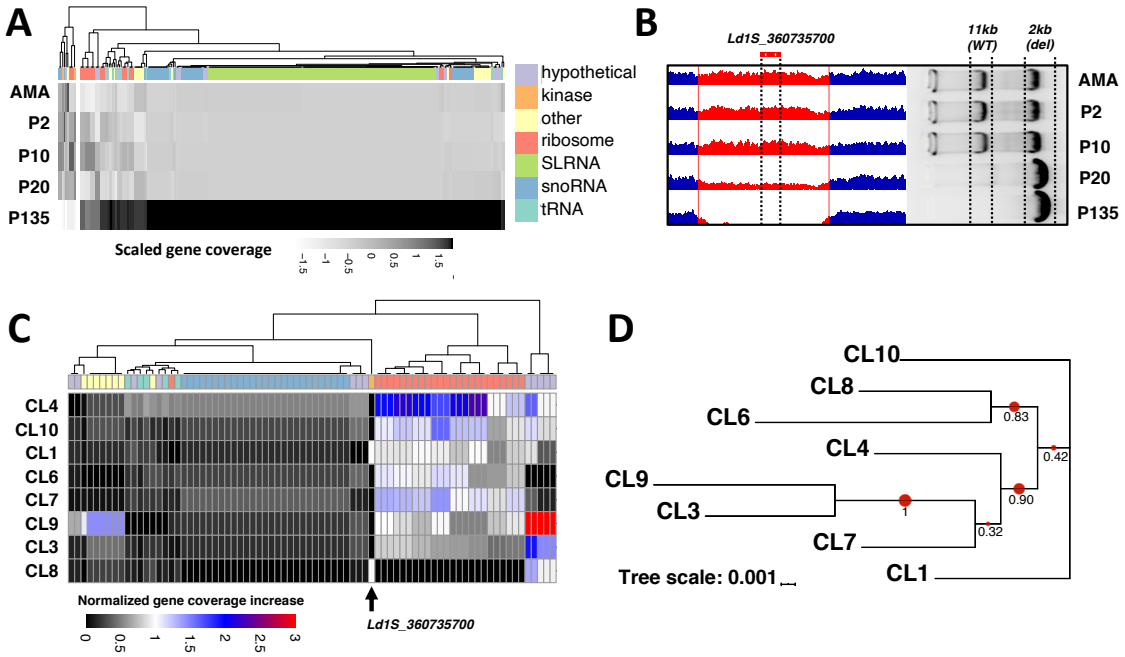

287
288 **Longitudinal analysis of gene CNVs during fitness gain in culture.** (**A**) Heatmap generated by
289 plotting gene read depth values (columns) across *L. donovani* amastigotes isolated from infected
290 hamster spleen (AMA) and derived promastigotes evolving in continuous culture for 2, 10, 20 and
291 135 passages (P2, P10, P20, P135) (rows). The gray level reflects the scaled normalized gene
292 coverage as indicated in the figure. (**B**) Screenshot of the IGV genome browser showing gradual
293 loss of the NIMA-like kinase gene Ld1S_360735700 during culture adaptation between splenic
294 amastigotes (AMA), and derived promastigotes at passages P2 and P135. The right panel shows
295 the gel-electrophoretic analysis of PCR fragments obtained from lesion amastigotes (AMA) and
296 derived promastigotes at the indicated culture passages that are diagnostic for the WT (11kb) and
297 the deleted NIMA-like kinase locus (2kb). (**C**) Heatmap generated by plotting gene read depth
298 variation (columns) across eight clones isolated from the P20 population (rows). The color code is
299 defined in the legend and corresponds to the deviation from the minimum sequencing coverage
300 measured for that gene in all clones. The colored ribbon indicates the simplified gene annotation

301 as shown in the legend of panel A. The deletion of the NIMA-like kinase Ld1S_360735700 is
302 indicated by the arrowhead. (**D**) Analysis of the phylogenetic relation of the P20 clones. The red
303 dots and numbers indicate the node bootstrap support (1 = 100%). The genetic distance is indicated
304 by the branch length and scaled as indicated in the figure.
305

306 **Fig. 3**

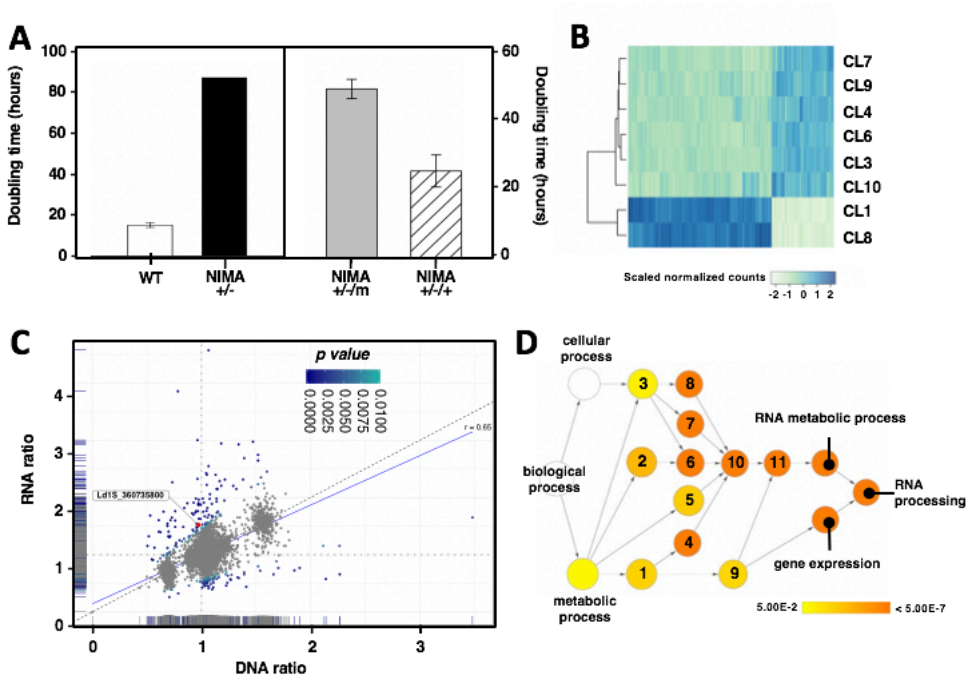

307
308 **Genetic and transcriptomic analyses of the NIMA-like kinase null mutant.** (**A**) Growth
309 analysis. WT and heterozygous NIMA +/- mutants generated by CRISPR/Cas9 gene editing (left
310 panel). Transgenic NIMA+/- parasites transfected with empty vector (NIMA+/-/m) or vector
311 encoding for the NIMA-like kinase gene (NIMA+/-/+) (right panel). The doubling time of parasites
312 in logarithmic culture phase is shown. (**B**) Heatmap of the scaled normalized RNAseq counts of
313 the genes differentially expressed in the P20 clones 1 and 8 (WT) with respect to the spontaneous
314 NIMA null mutant (spo-KO) clones 3, 6, 4, 7, 9, 10. A log2 fold change > 0.5 with adjusted p-
315 value < 0.01 was considered significant. Darker levels of blue reflect higher expression levels as
316 indicated by the legend. (**C**) Double-ratio scatter plot. The plot represents the ratio of the mean
317 DNA (*x*-axis) and RNA (*y*-axis) sequencing read counts between the clones that lost the NIMA-
318 kinase gene (CL3-4-6-7-9-10) and the NIMA-kinase wild-type clones (CL1 and CL8). Each dot
319 represents an individual gene. The marginal distributions for DNA and RNA ratio values are
320 displayed along the *x*- and *y*-axes. The color indicates the statistical significance level of the genes'
321 double-ratio scores (*i.e.* RNA ratio divided by DNA ratio) as indicated in the legend. The NIMA-

322 like kinase homolog Ld1S_360735800 is labeled in red. The vertical and horizontal dotted lines
323 indicate DNA and RNA ratio values of 1, while the diagonal dashed line specifies the bisector.
324 The blue line represents a linear regression model built on the DNA and RNA ratio values and
325 measuring a Pearson correlation value of 0.65. (**D**) Functional enrichment analysis of the biological
326 process Gene Ontology (GO) terms for all genes in panel C showing a statistically significant
327 double-ratio score. The node color mapping is ranging from yellow to dark orange to represent
328 increasing significance levels, or lower adjusted p-values. White nodes are not significant. 1:
329 organic substance metabolic process, 2: nitrogen compound metabolic process, 3: cellular
330 metabolic process, 4: organic cyclic compound metabolic process, 5: primary metabolic process,
331 6: cellular nitrogen compound metabolic process, 7: heterocycle metabolic process, 8: cellular
332 aromatic compound metabolic process, 9: macromolecule metabolic process, 10: nucleobase-
333 containing compound metabolic process, 11: nucleic acid metabolic process.
334

Fig. 4:

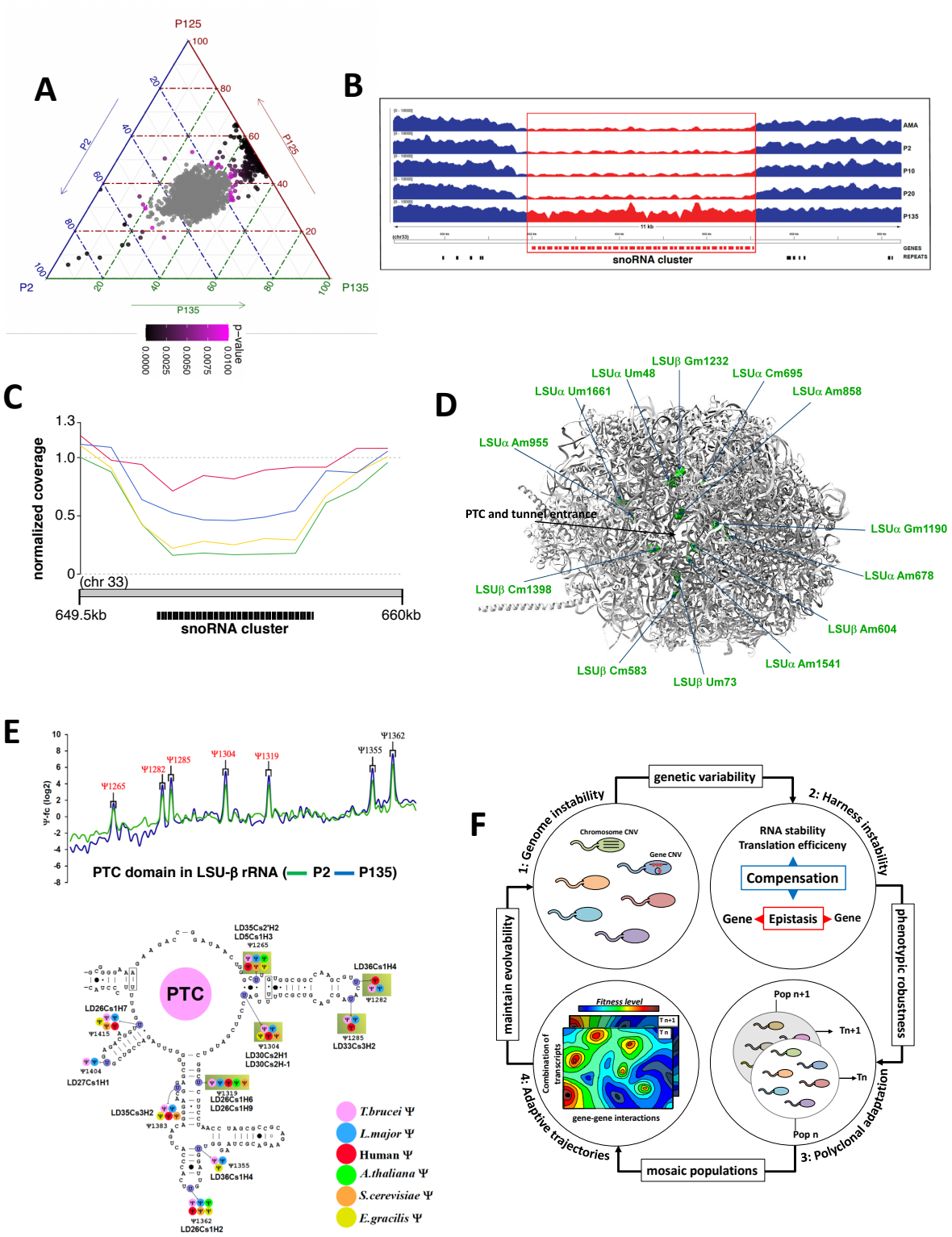
A
P125
P2
P135
p-value
0.0000
0.0025
0.0050
0.0075
0.0100
B
AMA
P2
P10
P20
P135
snoRNA cluster
GENES
REPEATS
C
normalized coverage
(chr 33)
649.5kb
660kb
snoRNA cluster
D
LSUβ Gm1232
LSUα Um48
LSUα Cm695
LSUα Um1661
LSUα Am858
LSUα Am955
PTC and tunnel entrance
LSUα Gm1190
LSUα Am678
LSUβ Cm1398
LSUβ Am604
LSUα Am1541
LSUβ Cm583
LSUβ Um73
E
Ψ-fc (log2)
Ψ1265
Ψ1282
Ψ1285
Ψ1304
Ψ1319
Ψ1355
Ψ1362
PTC domain in LSU-β rRNA (P2 P135)
PTC
LD35Cs2'H2
LD5Cs1H3
Ψ1265
LD36Cs1H4
Ψ1282
LD26Cs1H7
Ψ1415
Ψ1304
LD30Cs2H1
LD30Cs2H-1
Ψ1285
LD33Cs3H2
Ψ1404
LD27Cs1H1
Ψ1319
LD26Cs1H6
LD26Cs1H9
LD35Cs3H2
Ψ1383
Ψ1355
LD36Cs1H4
Ψ1362
LD26Cs1H2
T.brucei Ψ
L.major Ψ
Human Ψ
A.thaliana Ψ
S.cerevisiae Ψ
E.gracilis Ψ
F
genetic variability
1: Genome instability
2: Harness instability
Chromosome CNV
Gene CNV
RNA stability
Translation efficiceny
Compensation
Gene
Epistasis
Gene
maintain evolvability
phenotypic robustness
Fitness level
Combination of transcripts
gene-gene interactions
Pop n+1
Tn+1
Tn
Pop n
4: Adaptive trajectories
3: Polyclonal adaptation
mosaic populations

337 **snoRNA genes are amplified in long-term adapted parasites and promote rRNA**
338 **modification.** (**A**) Ternary plot showing for each gene the relative abundance in culture passage
339 P2 – P125 and P135. The axes report the fraction of the normalized gene coverage in each sample,
340 with each given point adding up to 100. Dots with color ranging from pink to black indicate
341 significant gene CNVs (p-value < 0.001). (**B**) Recovery of the snoRNA gene cluster CNVs during
342 culture adaptation. The panel illustrates a genome browser representation of the sequencing depth
343 measured in the samples at the indicated passage. Gene annotations and the predicted repetitive
344 elements are indicated. (**C**) Line plot showing the normalized sequencing coverage (y-axis) over
345 the snoRNA cluster region on chromosome 33 (x-axis) for the amastigote sample (AMA, green)
346 and three independent amastigote isolates (AMAH154, red; AMA07142, yellow; AMA1992, blue)
347 obtained from different hamster infections. (**D**) Hypermodified Nm sites are located around the
348 functional domains of the ribosome. The complete stoichiometry of each Nm site was measured
349 by RiboMeth-seq in P2 and P135 *L. donovani* strains as presented in **Table S20**. The
350 hypermodified Nm sites are highlighted in green and their identity is indicated on the 3D structure
351 of the *L. donovani* large subunit ribosome based on the previously deposited cryo-EM coordinates
352 (Protein Data Bank (*39*) accession 6AZ3) (*40*). The location of the PTC and mRNA entrance tunnel
353 are shown. (**E**) Hypermodified Ψs are present in the functional domains of the ribosome. The
354 relative changes in Ψ level was measured using Ψ-seq and is presented in **Table S21**.
355 Representative line graph of the fold change in rRNA pseudouridinylation level (Ψ-fc, log2) is
356 presented for P2 (green line) and P135 (blue line) for the PTC domain in LSU- Ψ rRNA. The
357 positions where the Ψ level is increased in four replicates are indicated in red. The location of Ψ
358 sites in the rRNA is depicted on the *Trypanosoma brucei* secondary structure (*19*). Hypermodified
359 sites are highlighted in boxes. The snoRNA guiding on each Ψ is indicated. The color code for

360 each Ψ site is indicative of the organism where it was already reported. (**F**) Model of *Leishmania*
361 polyclonal adaptation. (1) *Leishmania* intrinsic genome instability generates constant genetic
362 variability. (2) Epistatic interactions between gene CNVs and compensatory responses at the level
363 of RNA stability and translation efficiency eliminate toxic gene dosage effects and harness genome
364 instability. (3) This mechanism generates phenotypic robustness while at the same time
365 maintaining genetic variability, thus allowing for polyclonal adaptation. (4) The genetic mosaic
366 structure allows for distinct adaptive trajectories (T) inside and in-between adapting populations,
367 a process that conserves genetic heterogeneity and thus evolvability of the population despite
368 constant selection.
369

Supplementary Materials for

Genome instability drives epistatic adaptation in the human pathogen *Leishmania*

Giovanni Bussotti[1,2], Laura Piel[2], Pascale Pescher[2], Malgorzata A. Domagalska[3], K. Shanmugha Rajan[4], Smadar Cohen-Chalamish[4], Tirza Doniger[4], Disha-Gajanan Hiregange[5], Peter J Myler[6-10], Ron Unger[4], Shulamit Michaeli[4], and Gerald F. Späth[2,*]

Correspondence to: Gerald.spaeth@pasteur.fr

This PDF file includes:

Materials and Methods
Figs. S1 to S14
Captions for Data S1 to S21

Other Supplementary Materials for this manuscript include the following:

Data S1 to S21

[**Table S1: Mapping statistics of the dataset for the 204 clinical isolates.**

Table S2: Position and normalized coverage values of the collapsed CNV regions.

Table S3: Repetitive elements.

Table S4: Most positive and most negative LdBPK gene coverage correlations.

Table S5: Correlation map data.

Table S6: Correlation network data.

Table S7: Network hub genes.

Table S8: Collapsed CNVs showing highest read depth in the 204 L. donovani field isolates.

Table S9: Genes amplified in phylogenetically distinct clades.

Table S10: Normalized gene coverage values across ISC samples.

Table S11: Polysomy level analyses of two sets of Ld1S samples: (i) AMA to P135 isolates; (ii) four AMA isolates.

402 **Table S12: Ld1S annotation.**

403 **Table S13: Definitions of gene clusters in two sets of Ld1S samples: (i) AMA-P135 isolates;**

404 **(ii) P20 clones isolates.**

405 **Table S14: Gene CNVs and cluster CNVs detected during Ld1S culture adaptation.**

406 **Table S15: Gene CNVs and cluster CNVs detected in the eight Ld1S P20 clones.**

407 **Table S16: Single nucleotide variants (SNVs) in Ld1S P20 clones.**

408 **Table S17: Data of the differential expression analysis.**

409 **Table S18: DNA and RNA double-ratio data.**

410 **Table S19: P125/P135 gene coverage ratio values.**

411 **Table S20: The complete stoichiometry of Nm sites in *L. donovani* rRNA.**

412 **Table S21: The relative fold-change of Ψs in *L. donovani* rRNA between P135 and P2**

413 **parasites.**]

414
415
416
417

418 **Materials and Methods**

419 ***L. donovani* strains, culture conditions and cell cloning**

420 Culture-adapted *L. donovani* field isolates maintained for more than 20 *in vitro* passages (P) from
421 the Indian Sub-Continent (ISC) and previously subjected to whole genome sequencing analysis
422 were used in our study (*12*). *Leishmania (L.) donovani* strain 1S2D (MHOM/SD/62/1S-CL2D)
423 (Ld1S) was obtained from Henry Murray, Weill Cornell Medical College, New York, USA and
424 maintained by serial passages in hamsters. Amastigotes were recovered from infected hamster
425 spleen and differentiated into promastigotes in M199 medium supplemented with 10% FCS,
426 25mM HEPES pH 6.9, 4mM $NaHCO_3$, 1 mM glutamine, 1x RPMI 1640 vitamin mix, 0.2 µM
427 folic acid, 100 µM adenine, 7.6 mM hemin, 8 µM biopterin, 50 U ml^{-1} of penicillin and 50 µg ml^{-}
428 ^{1} of streptomycin. Promastigotes were serially passaged once stationary phase was reached for
429 either 2, 10, 20, or 135 passages corresponding to respectively 20, 60, 190, and 3,800 generations.
430 An independent *L. donovani* isolate was grown in culture for over 33 months until P125
431 (corresponding to approximately 3,500 generations). Three independent splenic amastigotes
432 populations were recovered from as many infected hamsters using the same culture conditions.
433 Serial dilutions of passage 20 (P20) promastigotes were plated on M199 Agar plates and 8 clones
434 were recovered and expanded for 2 passages in liquid culture (*10*).

435

436 **Nucleic acid extraction and deep sequencing**

437 All sequencing analyses were performed using Illumina short-read technology. DNA extraction
438 and sequencing protocols of the *L. donovani* field isolates from the Indian Sub-Continent (ISC)
439 are described in (*12*) DNA extraction and sequencing analysis of *L. donovani* LD1S amastigotes
440 (AMA) and derived promastigotes at passages P2, 10, and 20 are described in (*10*). For new
441 amastigote isolates (AMAH154, AMA1992, AMA07142) and promastigote strains (P125, P135),

442 DNA extractions were performed using DNeasy blood and tissue kits from Qiagen according to
443 the manufacturer's instructions. Nucleic acid concentrations were measured and the DNA quality
444 was evaluated by measuring the OD ratios 260/280 and 260/230 and by agarose gel-
445 electrophoresis. Between 2 to 5µg of DNA were used for sequencing.

446 For samples AMAH154, AMA1992, AMA07142, P125 and P135, short-insert, paired-end
447 libraries were prepared with the KAPA Hyper Prep Kit (Kapa Biosystems). The libraries were then
448 sequenced using TruSeq SBS kit v3-HS (Illumina Inc., CA, USA). Multiplex sequencing was
449 performed using HiSeq 2000 flowcell v3, generating 2×101bp paired-end reads, according to
450 standard Illumina procedures. Reads were deposited in the Sequence Read Archive (SRA)
451 database (*37*) and are publicly available under accession no PRJNA605972**.**

452

453 **Whole genome sequencing data analysis**

454 Genomic reads were aligned and the nucleotide sequencing depth was measured and normalized
455 as previously described (*41*). For the genome-wide detection of CNVs across the 204 ISC isolates,
456 the LdBPKv2 reference genome was partitioned into adjoining intervals of a fixed length of 300bp
457 (bins), and the depth of coverage of each bin was measured and compared across samples. The
458 mean sequencing coverage normalized by the median chromosome coverage was computed for
459 each bin as already described (*41*). In **Fig. 1A** and **1B** and to compute the genome fraction of
460 amplified or depleted regions, all maxi-circle DNA bins as well as the bins with a median
461 normalized coverage > 0.01 but mean read mapping quality score (MAPQ) < 50 were discarded.
462 We referred to genomic bins as being deleted, depleted or amplified respectively for normalized
463 sequencing coverage values ≤ 0.01, < 0.5 and > 1.5. **Fig. 1B** shows the copy number variant bins
464 across the samples. To account for differences in ploidy levels, the bin copy number was evaluated

465 as the bin sequencing coverage normalized by the chromosome median sequencing coverage (i.e.
466 copy number per haploid genome). Bins showing a copy number variation of at least 1 across the
467 204 ISC isolates were considered in the analysis. The heatmap color scale reflects the difference
468 in bin normalized read depth with respect to the minimum value measured across all genomes.
469 Black indicates no variation. White, blue and red correspond to increases in normalized coverage
470 levels of respectively 1, 2 and 3. Coverage variations greater than 3 were down sized to 3. The
471 analyses shown in **Fig. 1F** and **1G** rely on CNV regions potentially spanning multiple genomic
472 bins aggregated into individual larger units. We refer to such grouped bins as "collapsed bins".
473 Groups of genomic CNV bins separated by less than 1,200 bases were merged together, and their
474 normalized sequencing coverage averaged. To account for potential unannotated UTR regions in
475 **Fig. 1F** and **1G**, CNV regions were considered intergenic if located at a distance of at least 100bp
476 from annotated genes. The line plot in **Fig. 4C** illustrates the sequencing coverage in 1,000bp long
477 bins normalized by chromosome 33 median sequencing coverage.

478 Likewise, sequencing coverage was used to estimate and compare gene copy numbers. The
479 mean sequencing coverage of each gene was estimated and normalized as previously published
480 (*41*). Reads with a mean MAPQ score < 50 were filtered because not directly quantifiable with the
481 sequencing technology we used. Genes with a variation of normalized coverage > 1 in the 204
482 field isolates were considered to be copy number variant. The heatmap in **Fig. 1E** includes the
483 genes (rows) showing convergent amplification (normalized coverage > 1.5) across 191 ISC core
484 group (*12*) isolates (columns). Genes amplified only in isolates sharing a common ancestor were
485 excluded from the analysis. **Fig. 2A**, **2C, 4A** and **S9** show gene copy number variations across
486 different data sets. Genes supported by reads with and average MAPQ score < 50 were grouped
487 into clusters based on sequence similarity, quantified as cluster entities and evaluated for possible

488 variation across samples (gene cluster CNVs). Briefly, the stranded sequences of low MAPQ genes
489 were grouped with cd-hit-est (version 4.6.8) (*42*) with options "-s 0.9 -c 0.9 -r 0 -d 0 -g 1" selecting
490 clusters of highly similar genes. Samtools view (version 1.3) and BEDTools coverage (version
491 2.25.0) were used to measure the mean sequencing depth of the individual low MAPQ genes and
492 were run, respectively, with options "-F 1028" and "-d -split". For the mean coverage estimate
493 possible intragenic gap regions were not considered. The mean coverage of each gene was
494 normalized by the median coverage of its chromosome. Eventually, the normalized mean coverage
495 of all genes in a cluster was averaged to compute the cluster support. **Fig. 2A** shows the gene and
496 cluster increasing in copy number between amastigote (AMA) and P135, using as a cutoff an
497 increment in normalized coverage of at least 0.5. **Fig. 2C** represents the gene and cluster CNV
498 detected in the clones using as a cutoff a minimum variation in normalized coverage of at least
499 0.5. Black indicates no variation. White, blue and red reflect increasing values in normalized
500 coverage levels of respectively 1, 2 and 3. Coverage variations greater than 3 were down sized to
501 3. For the analysis illustrated in **Fig. 4A** the coverage of each gene was evaluated as the number
502 of mapping reads excluding duplicates, increased by a pseudo-count of 1, and normalized by the
503 median number of reads per gene in the respective samples. In **Fig. S9** the mean gene sequencing
504 coverage values were normalized by the median of the mean gene coverage values in the respective
505 P125 and P135 samples. The genes with mean MAPQ < 50 in either sample were discarded.

506 To represent the sequencing coverage of selected genes and genomic areas we used the
507 Integrative Genomics Viewer (IGV) (*43*). In **Fig. 2B**, **4B**, **S6B** and **S7A** the sequencing coverage
508 tracks were produced with bamCoverage from the deepTools suite (*44*) (version 2.4.2) with
509 options "--binSize 10 --smoothLength 30" and ignoring duplicated reads. Normalization of reads

510 per kilobase per million reads (RPKM) was applied on separate chromosomes to render the
511 coverage comparable across samples and ploidy levels.

512 We determined chromosome aneuploidy in our samples sets based on sequencing coverage.
513 In **Fig. S6A** and **S10,** the normalized sequencing coverage was binned in contiguous 2,500bp
514 windows for each sample and for each chromosome, and the distribution of the windows' mean
515 coverage scores were displayed. Sequenced positions where more than 50% of the reads showed
516 a MAPQ lower than 50 were not considered in the analysis. To estimate chromosome copy number
517 differences, the window coverage was normalized by the median coverage of the chromosome
518 showing a stable disomic level across samples (chromosomes 21-25 respectively for **Fig. S6A** and
519 **S10**) and multiplied by two. The distribution of the mean window coverage was compared with
520 the R (*45*) Wilcoxon test and the p-values of the comparisons are reported in **Table S11**.

521

522 **Reference genomes**

523 The analyses regarding the use of the Sudanese *L. donovani* strain 1S2D (Ld1S) were performed
524 utilizing its PacBio genome assembly available from the NCBI website under the biosample (*46*)
525 accession n° SAMN07430226 and the bioproject (*46*) accession n° PRJNA396645. To produce
526 Ld1S genome annotation we combined different approaches. We ran the Companion pipeline (*47*)
527 without using transcript evidence and exploiting *L. major* Friedlin as a reference organism to
528 specify the models for gene finding and functional annotation transfer. The predicted gene
529 identifiers were renamed to match chromosomal localization. Then we complemented Companion
530 annotations with LdBPKv2 (*7*) homology-based predictions. We used NCBI-tblastn (version
531 2.2.28) (*48*) to search the amino acid sequence of LdBPKv2 genes with an e-value threshold of
532 0.01. To enable the screening of non-coding sequences we also ran gmap (version 2015-07-23)

533 with options "--npaths 30 --no-chimeras --nosplicing –prunelevel --min-trimmed-coverage 0.9 --
534 min-identity 0.9" searching Ld1S homologs of all LdBPKv2 genes. All the significant NCBI-
535 tblastn and gmap predictions that were not overlapping on the same strand with Companion
536 annotations were retained. BEDTools merge (version 2.25.0) was used to combine overlapping
537 predictions into single gene annotations spanning all of the combined predictions. Eventually
538 NCBI-blastn was used to search in the Ld1S intergenic space the *Leishmania major* Friedlin
539 UsnRNA, snoRNA, SLRNA and 7SL non-coding RNA classes. Overall, the Ld1S genome
540 encodes for 10,532 genes: 8,850 defined by the Companion pipeline, 104 defined by homology
541 with LdBPKv2 genes, and 1,578 defined by homology with *L. major* Friedlin ncRNA classes.

542 Ld1S gene functions were inferred adopting a hierarchical approach. Firstly, we transferred
543 the function of *L. donovani* strain BPK282A1 (LdBPK282A1) homolog genes available from
544 TriTrypDB (*49*) (downloaded the 05/07/2019). To this end, OrthoFinder (*50*) (version 2.2.7) was
545 used with the DIAMOND (*51*) search program to establish orthology relation between
546 LdBPK282A1 (downloaded from the Sanger FTP server
547 ftp://ftp.sanger.ac.uk/pub/project/pathogens/ on the 12/10/2018) and Ld1S gene annotations.
548 NCBI-blastn was run with options "-dust no -soft_masking false -evalue 10" to scan and try to
549 rescue the low complexity genes were OrthoFinder failed to determine homology. When "one-to-
550 many" homologs occurred (i.e. one Ld1S gene matching multiple significant LdBPK282A1
551 homologs), the function of all individual homologs was concatenated in a single, not-redundant
552 functional assignment. For the genes lacking functional annotation, or reported as "hypothetical
553 proteins" we assigned the function reported in the Companion GAF output file or the transcript
554 type if no description was available. Then, if no annotation was found other than "hypothetical
555 proteins", we sought to infer the gene function using HMMer (*52*) (version 3.1b2) to scan the gene
556 protein sequences against EGGNOG kinetoplastida database (*53*) (version 4.5)

557 (http://eggnogdb.embl.de/download/eggnog_4.5/data/kinNOG/), and ultimately combining the
558 annotated functions in EuPathDB (*54*) and UniProt (*55*) (downloaded the 20/09/2019). To extract
559 the UniProt function annotations we queried the Gene Ontology Annotation (GOA) (*56*) database
560 with the Uniprot identifiers of the LdBPK282A1 homologs of Ld1S genes.

561 In order to assign the Gene Ontology Identifiers (GO IDs) we combined the GOA-derived
562 identifiers with the ones available from the corresponding orthologs in target species: LdBPK, *L.*
563 *infantum*, *L. major*, *L. mexicana*, *Typanosoma brucei brucei 927* (Tbru) and *Typanosoma cruzi*
564 (Tcru). For each target species we retrieved both the "curated" and "computed" GO IDs from
565 TriTrypDB on the 11/09/2019. OrthoFinder with the DIAMOND search program was applied to
566 establish orthology between the genes in Ld1S and in target species. In "one-to-many" orthology
567 relations we concatenated all the non-redundant GO IDs from all the homologs. The GO IDs were
568 then assigned based on the hierarchy: LdBPK curated > LdBPK GOA > *L. infantum* curated > *L.*
569 *major* curated > *L. mexicana* curated > Tbru curated > Tcru curated > LdBPK computed > *L.*
570 *infantum* computed > *L. major* computed > *L. mexicana* computed > Tbru computed > Tcru
571 computed. The GO IDs were assigned if not present in any higher rank GO ID data set. The GO
572 IDs of snoRNAs, UsnRNA, SLRNA and 7SL classes defined by homology with *L. major* Friedlin
573 genes were manually attributed. Overall, we assigned biological process (BP), molecular function
574 (MF) and cellular component (CC) GO IDs to 5,246, 4,521 and 7,236 Ld1S genes.

575 All analyses regarding the 204 Indian sub-continent (ISC) isolates (*12*) used the Nepalese
576 PacBio *L. donovani* (LdBPKv2) genome and annotation as reference (*7*). LdBPKv2 gene function
577 was inferred adopting a hierarchical approach similar to the one described for Ld1S. Higher
578 priority was given to TriTrypDB, followed by Companion GAF (available from (*7*)) and
579 EGGNOG functional annotations.

580

581 **Repeat analysis**

582 We annotated the repetitive elements in the LdBPKv2 genome producing a comprehensive dataset
583 (**Table S3**). To build this dataset, we merged the repetitive elements identified by different
584 approaches in three distinct repeat sets and present with at least 5 copies in the genome.

585 The first set of repetitive elements accounts for the interspersed repeat elements predicted
586 with RepeatMasker (*57*) (version 4.0.8) with options "-e crossmatch -gff -xsmall -s", scanning the
587 genome to identify short simple/low complexity repetitive elements and interspersed repetitive
588 elements. RepeatMasker was run in combination with the Repbase (*58*) library to identify
589 *Leishmania*-specific and ancestral repeats, and with the output of RepeatModeler (version 1.0.11)
590 (*59*), a pipeline to identify transposable elements run with option "-engine ncbi". Redundant,
591 RepeatModeler-defined elements overlapping with Repbase elements were discarded.
592 RepeatMasker output was processed collapsing self-inclusive low-complexity motifs to the
593 shortest identical sub-motif (e.g. TAGTAG -> TAG) and merging together overlapping repeats
594 elements of the same type (**Table S3**).

595 The second set of repetitive elements consists in the DNA motifs enriched at the boundaries
596 of the CNV regions we detected in the core group of 191 ISC *L. donovani* field isolates, excluding
597 the "Yeti" strains (*12*). Such boundaries were defined as the genomic regions spanning 1kb and
598 flanking both sides of each CNVs. The CNVs defined in the core group include the 300bp genomic
599 bins with average read MAPQ score > 50, and showing a variation of normalized sequencing
600 coverage score > 1 in the sample set. The bins localized within 6kb were collapsed and their
601 sequencing scores averaged. Significant DNA motifs were detected using MEME (version 5.0.4)
602 (*60*) with option "-dna -revcomp -nmotifs 20 -evt 0.01 -mod anr" and specifying a custom

603 background model of order 3 with fasta-get-markov, a tool included in the MEME suite. The
604 sequences we used to build such background model were randomly extracted from the LdBPKv2
605 genome with BEDTools shuffle (*61*) (version 2.25.0) in order to resemble the ones scanned by
606 MEME in terms of number and size, but not including them. The DNA motifs predicted with
607 MEME were then mapped genome-wide with MAST using the options "-hit_list -comp -remcorr
608 -mt 0.0000001".

609 The third set of repetitive elements includes the DNA motifs enriched at the boundaries of
610 tandem repeat cluster (TRC) regions. TRCs are characterized by the tandem repetition of large
611 genomic segments. To detect TRCs in the LdBPKv2 genome we streamlined a pipeline including
612 several steps and relying on several bioinformatics tools. First, we detected inexact repetitive
613 elements on individual chromosomes. For this purpose we ran nucmer (version 3.23) (*62*) with
614 options "--maxmatch --nosimplify", and show-coords (version 3.23) (*62*) with options "-r -T -o -l
615 -d -I 80 -L 50". Possible overlapping predictions were collapsed with BEDTools merge (*61*). To
616 remove distantly related elements the resulting elements were re-clustered by sequence similarity
617 with cd-hit-est (version 4.6.8) with options "-d 0 -g 1". Then to refine the element boundaries we
618 compared all-versus-all sequences in each cluster with NCBI-blastn (version 2.2.28) (*48*) with
619 options "-dust yes -soft_masking true -evalue 0.01", retaining the elements longer than 50bp. Next,
620 we processed each cluster grouping the sequences based on a maximum distance cutoff of 2kb,
621 thus ensuring that the repetitive element occur in the same genomic area. Then the clusters found
622 to be intersecting each other were pooled together to generate the TRCs. Eventually the TRCs were
623 processed enforcing a minimum distance between an element and the one downstream of at least
624 100bp. The genomic space between the elements inside the TRC and the regions of 1kb flanking

625 each TRC were evaluated to identify enriched DNA motifs. Significant motifs were detected with
626 MEME and mapped genome-wide with MAST as already described for the CNV boundaries.
627
628 **CNV association analyses**
629 We evaluated weather LdBPKv2 CNVs are significantly associated with genes and intergenic
630 regions utilizing GAT (*63*), a tool for testing the significance of overlap of genomic intervals. In
631 this analysis we considered 10,000 simulations in which we assigned random positions to the
632 collapsed bin CNV regions. For each simulation we evaluated the number of nucleotides
633 overlapping the gene and intergenic regions, thus implementing the null models that the CNV set
634 of intervals is placed independently. The genomic regions accessible for simulation include (i) the
635 36 chromosomes of the LdBPKv2 genome, excluding the assembly gaps, (ii) the genomic positions
636 where more than 50% of the reads have a MAPQ < 50, and (iii) the regions shorter than 20kb not
637 containing any CNV. To account for possible non-annotated UTR elements, we expanded the gene
638 coordinates by 100bp on both sides, and consequently shrunk the intergenic regions.
639 GAT was also used to determine the association between the LdBPKv2 CNV boundaries
640 and the comprehensive repeat dataset. For each of the 10,000 simulations we evaluated the number
641 of CNV boundaries overlapping each repeat type. For this purpose, all low-complexity motifs were
642 collectively considered as a single class named "simpleRepeats". The CNV boundaries included a
643 1kb area flanking the CNV, plus the segments of 150bp spanning from the CNVs extremities and
644 moving toward their center. Eleven repeat types were found significantly associated to CNV
645 regions (**Fig. 1C**).
646
647 **Network analysis**

648 To explore the interaction between gene CNVs we performed a network analysis. In the graph
649 shown in **Fig. 1D,** the edges indicate significant gene CNVs correlation with adjusted p-value
650 lower than 0.01. Nodes, representing the gene CNVs, are colored according to the MCL clustering
651 (R package version 1.0) (*64*) of the gene CNVs absolute correlation values. The clustering was
652 performed using respectively 2 and 3 for the expansion and inflation MCL parameters. The
653 centroid and the standard deviation were computed for each cluster. Nodes mapping more than 2
654 standard deviations away from the cluster centroid were labeled as outliers and not shown. The
655 network was produced using the R library igraph (R package version 1.1.2) (*65*), using the
656 "layout_with_fr" function, placing vertices on the plane using the force-directed layout algorithm
657 by Fruchterman and Reingold (*66*).
658
659 **Phyogenetic analysis**
660 The phylogenetic tree in **Fig. 1E** and the cladogram in **Fig. S5** include respectively the 191 ISC
661 core isolates and the full 204 ISC set (*12*) and were calculated with raxmlHPC-PTHREADS
662 (version 8.2.8) (*67*) with options '-m ASC_GTRGAMMA --asc-corr=lewis', with 10 starting trees
663 and 10,000 rapid bootstrap runs. The program was run providing single nucleotide variant (SNV)
664 positions returned by freebayes (version v1.0.1-2-g0cb2697) (*68*), and further filtered to produce
665 high-quality predictions. Freebayes was run with options "--no-indels --read-indel-limit 0 --no-
666 mnps --no-complex --read-mismatch-limit 3 --read-snp-limit 3 --hwe-priors-off --binomial-obs-
667 priors-off --allele-balance-priors-off --min-alternate-fraction 0.05 --min-base-quality 5 --min-
668 mapping-quality 50 --min-alternate-count 2 --pooled-continuous". Then the variants mapping to
669 the maxi-circle DNA or presenting multiple alternate alleles were discarded. Additionally, all
670 variants with an alternate allele frequency < 0.9 were removed. Next, SNV predictions where the
671 mean MAPQ of the reads supporting the alternate or the reference allele was < 20 were also

672 removed. We filtered SNVs with sequencing coverage above or below 4 median absolute
673 deviations (MADs) from the median chromosome coverage. Eventually, SNVs mapping inside
674 homopolymers were filtered as described (*41*). To ease the visualization, the branch representing
675 the reference genome was removed from the tree and the cladogram. The phylogenetic tree and
676 the associated gene CNV heatmap were displayed with the R library ggtree (version 2.0.1) (*69*). A
677 similar raxmlHPC-PTHREADS/freebayes approach was adopted to determine the evolutionary
678 relationship between the P20 clones (**Fig. 2D**). As compared to the analyses in **Fig. 1E** and **S5**, we
679 increased the number of starting trees (10,000), used 10,000 standard bootstrap iterations, loosened
680 the stringency of the alternate allele frequency filtering (< 0.1), and displayed the tree with iTol
681 (version 5) (*70*).
682
683 **RNAseq analysis**
684 RNA was prepared and RNA sequencing (RNAseq) performed using an Illumina Hiseq 2000
685 platform and TruSeq v3 kits as previously described (*10*) We assessed the statistical significance
686 of quantitative gene expression differences between WT clones and spontaneous NIMA-like
687 kinase null mutant clones (spo-KO) with DESeq2 (version 1.14.1) (*71*). Genes with an adjusted p-
688 value < 0.01 and a log2 fold change above 0.5 or below -0.5 were deemed differentially expressed.
689 Maxi-circle DNA genes were not considered in the analysis. The gene expression was quantified
690 by HTSeq (version 0.6.1) (*72*) while the reads were mapped as previously described (*41*).
691 To investigate post-transcriptionally regulated transcripts (**Fig. 3C**), we considered all the
692 genes excluding the ones with 0 RNAseq read counts and the ones encoded on the maxi-circle
693 DNAs. All HTSeq gene read counts estimated for RNAseq (RNA) and whole genome sequencing
694 (DNA) were incremented by 1 pseudocount. For RNA and DNA data, the mean read counts in

695 spo-KO clones was divided by the mean read counts in WT clones (representing the ratio scores
696 that are displayed respectively on the y- and the x-axes in **Fig. 3C**). Both the numerator and
697 denominator were normalized by the average library size (defined as the total number of reads
698 mapping on all genes). The double-ratio score was estimated as the ratio between the RNA and
699 DNA ratios. Genes with double-ratio score < 1 and p-value < 0.01 and were considered
700 "destabilized" (i.e. less RNA than expected considering the DNA amount). Genes with double-
701 ratio score > 1 and p-value < 0.01 were considered "stabilized" (i.e. more RNA than expected
702 considering the DNA amount).
703
704 **Gene Ontology (GO) term enrichment analysis**
705 Cytoscape (version 3.7.2) (*73*) was used in combination with *BiNGO* (version 3.0.3) (*74*) to detect
706 biological process GO terms enriched amongst the genes with significant double-ratio scores. In
707 **Fig. 3D** node color mapping is ranging from yellow to dark orange to represent increasing
708 significance levels, or lower adjusted p-values. White nodes are not significant. The BiNGO
709 analysis was run using the "go-basic.obo" ontology file (release 2019-10-07) (*75, 76*) available
710 from http://geneontology.org/docs/download-ontology/, and as a reference the set of 8,880 genes
711 reporting a mean of normalized counts taken over all samples > 0 ("baseMean" metric in the
712 DESeq2 analysis).
713
714 **PCR analyses**
715 The presence of a 10.3kb genomic deletion on chromosome 36 (coordinates 36:574,041 – 584,350)
716 comprising a conserved NIMA kinase homolog (LdBPK_361580.1) was monitored by PCR
717 amplification of a diagnostic fragment of 2kb. Briefly, genomic DNA was extracted from

718 amastigotes purified from hamster spleen (*77*) or logarithmic promastigotes in culture using the
719 DNeasy Blood and Tissue kit (Qiagen) according to manufacturer's instructions. DNA quality was
720 assessed by monitoring the 230/260 and 280/260 ratios and concentration was determined by
721 spectrophotometry measuring the absorbance at 260nm. Genomic DNA was subjected to PCR
722 analysis using LongAmp kit (New England Biolabs) according to the manufacturer's instructions.
723 Primers were designed targeting genomic sequence from either side of the deleted area (forward
724 primer (F): AGACAGACAGCAATGCGTGAT; reverse primer (R):
725 ACAGACGTCTGTCCGTGCTT) or the NIMA kinase open reading frame (F:
726 ATGTCGGGGGGTAACGCC; R: TCACTCCTTTGCGGGTAGAGCA). The PCR mix was
727 composed of 1x LongAmp Taq reaction buffer, 300µM dNTP each, 0.4µM of each primer, 10ng
728 of genomic DNA and 5 units of LongAmp Taq DNA polymerase. The thermal cycling conditions
729 were: initial denaturation at 94°C for 30s, followed by 30 cycles of 94°C for 30s, 60°C for 30s and
730 65°C for 10min. A final extension step was performed for 10min at 65°C.

731 PCR was performed for the CRISPR/cas9-mediated gene deletion assay. Based on the
732 sequence of the NIMA kinase target gene (LdBPK_361580.1), single-guide RNA (sgRNA) were
733 amplified using Expand High Fidelity polymerase (Roche) with 0.2mM dNTP each, 1x Expand
734 High Fidelity buffer with $MgCl_2$ (15 mM final concentration), 2µM each of primers G00 (sgRNA
735 scaffold) and either 5'-sgRNA primer
736 (gaaattaatacgactcactataggTAGAAAGAACGAAGTGATCGgttttagagctagaaatagc) or 3'-sgRNA
737 primer (gaaattaatacgactcactataggAAGAGGAAGAAGATCACCAAgttttagagctagaaatagc) in 20µl
738 final volume. PCR steps were: 30s at 98°C followed by 35 cycles of 10s at 98°C, 30s at 60°C, and
739 15s at 72°C. Sterilization of PCR products was performed at 94°C for 5min. PCR amplification
740 of the DNA donor was performed using 30ng of pT plasmid containing the blasticidin resistance

741 cassette as template (*78*). The PCR mix contained 0.2mM dNTP each, 1x Expand high Fidelity
742 buffer with $MgCl_2$ (3.375mM final concentration), 3% DMSO, 1 unit of Expand High Fidelity
743 polymerase and 2µM of each primer (F:
744 CTCTCCACCTCTGAATCTACTACGGTTTTCgtataatgcagacctgctgc; R:
745 CGCAAAGGGTGCCGCCACATCGCAAACGCGccaatttgagagacctgtgc) in 40µl final volume.
746 PCR steps were: 5min at 94°C followed by 40 cycles of 30s at 94°C, 30s at 65°C, 2min 15s at
747 72°C followed by a final elongation step for 7min at 72°C. Sterilization of PCR products was
748 performed at 94°C for 5 min.

749 For the heterozygote $NIMA^{+/-}$ null mutant, validation was performed by PCR amplification
750 of LdBPK_361580.1 open reading frame (NIMA_F and NIMA_R) using 10ng genomic DNA as
751 template and the amplification of the blasticidin resistance cassette (F: atgcctttgtctcaagaagaatc and
752 R: ttagccctcccacacataac) using the 11kb fragment surrounding the insertion locus (diagn_F and
753 diagn_R) as template.

754 For transgenic expression assay, the NIMA kinase gene LdBPK_361580.1 was PCR
755 amplified using the Expand high fidelity polymerase kit (Roche) and 30ng of genomic DNA of
756 promastigotes as template with primers F: ACCCTCGAGATGTCGGGGGGTAAC and R:
757 CGCCTTAAGTCACTCCTTTGCGGGTAGAG. The amplicon was first sub-cloned into pGEM-
758 T (Promega), validated by sequencing, and inserted into pXNG (kindly given by Stephen Beverley,
759 Washington University School of Medicine, St. Louis, MO, USA, (*79*)) to generate construct
760 pXNG-NIMA following digestion by XhoI and AflIII (*80*). For the validation of the pXNG
761 transfection in the heterozygote $NIMA^{+/-}$ null mutant, PCR assay was performed targeting the
762 nourseothricin resistance cassette (F: ACCGTCGACATGAAGATTTCGGTGAT; R:

763 CGGTCTAGATTAGGCGTCATCCTGT) after extraction of circular DNA from promastigotes at
764 logarithmic growth phase using the Nucleospin Plasmid kit (Macherey Nagel).
765
766 **Null mutant analysis**
767 Vector pTB007 was used, containing a T7 RNA polymerase gene, the humanized Streptococcus
768 pyogenes Cas9 gene, and homology regions allowing for stable integration into the beta-tubulin
769 locus (*78*). The plasmid was linearized with SbfI (NEB) and Hind-III (NEB) and dephosphorylated
770 using the Antarctic phosphatase (NEB) for 30min at 37°C. The 12kb-fragment was extracted and
771 purified from 0.8% agarose gel using the Wizard SV Gel and PCR clean-up system (Promega).
772 Transfection of P2 promastigotes from logarithmic growth phase was performed using a BioRad
773 Gene pulser (*81*). After centrifugation (1600*g*, 10min, room temperature), cells were resuspended
774 in Cytomix (0.15mM $Cacl_2$, 120mM KCl, 10mM KH_2PO_4, 5mM $MgCl_2$, 25mM HEPES (pH 7.5),
775 2mM EDTA (pH 7.6)) and 5.10^7 cells were electroporated by two pulses at 1,500V, 25µF, infinite
776 resistance. The next day, hygromycin B (Invitrogen) was added to select for transgenic cells
777 (30µg/ml final concentration). Virulence of the transgenic line (termed Ld1S PT007) was
778 maintained by two successive passages in hamsters as described (*77*) and recovered parasites were
779 grown in the presence of hygromycin B. To generate heterozygous $NIMA^{+/-}$ null mutants, Ld1S
780 PT007 promastigotes from logarithmic growth phase were transfected with the Biorad Gene Pulser
781 combining sterilized PCR constructs and sgRNA. After centrifugation (1600*g*, 10min, room
782 temperature), cells were resuspended in Cytomix and $3x10^7$ cells were electroporated using the
783 following conditions: 900V, 50µF, infinite resistance, two pulses. The next day, blasticidin S
784 hydrochloride (Sigma) was added to select for resistant cells (20 µg/ml final concentration) and
785 isolate heterozygous $NIMA^{+/-}$ null mutants.

786 To generate the addback control, NIMA$^{+/-}$ promastigotes from logarithmic growth phase were
787 transfected in electroporation buffer containing 90mM sodium phosphate, 5mM potassium
788 chloride, 0.15mM calcium chloride, 50mM HEPES, pH 7.3 (*82*) using the program X-001 of the
789 Amaxa Nucleofector IIb (Lonza) with either 5µg pXNG Mock or pXNG-NIMA DNA. For
790 selection of transfected cells, nourseothricin (Sigma) was added 24 hours after electroporation at
791 100µg/ml final concentration.
792

793 **Methylation (Nm) and pseudouridine (Ψ) rRNA modification analyses**

794 We quantitatively mapped the position of individual Nm sites in *L. donovani* rRNA based on
795 Cryogenic electron microscopy (Cryo-EM) (*40*) and mass-spectrometry (MS) (*83*) (**Table S20**).
796 The snoRNAs predicted to guide Nm site were identified by homology to *L. major* snoRNAs (*84*)
797 (**Table S20**). The relative methylation score (RMS score) of each individual Nm site was measured
798 for both cell culture P2 and P135 (**Table S20**). Three biological replicates of P2 and two biological
799 replicates of P135 were used for the analysis.

800 The fold change of Ψ–ratio between the reads obtained from Ψ-seq (*19*) at specific modification
801 sites after and before 1-Cyclohexyl-3-(2-morpholinoethyl)carbodiimide metho-p-
802 toluenesulfonate, 95%, ACROS Organics™ (CMC) (Fisher Scientific Acros 111360050)
803 treatment of P135/P2 (**Formula 1**) was calculated across the rRNA based on four independent
804 replicates. Only sites with log2 fold change >1.3 in all replicates were considered as
805 hypermodified.

806 $$P135\ \log_2(+CMC/-CMC)/P2\ \log_2(+CMC/-CMC)$$
807
808 **Formula 1.** Fold change of Ψ–ratio.
809

Fig. S1

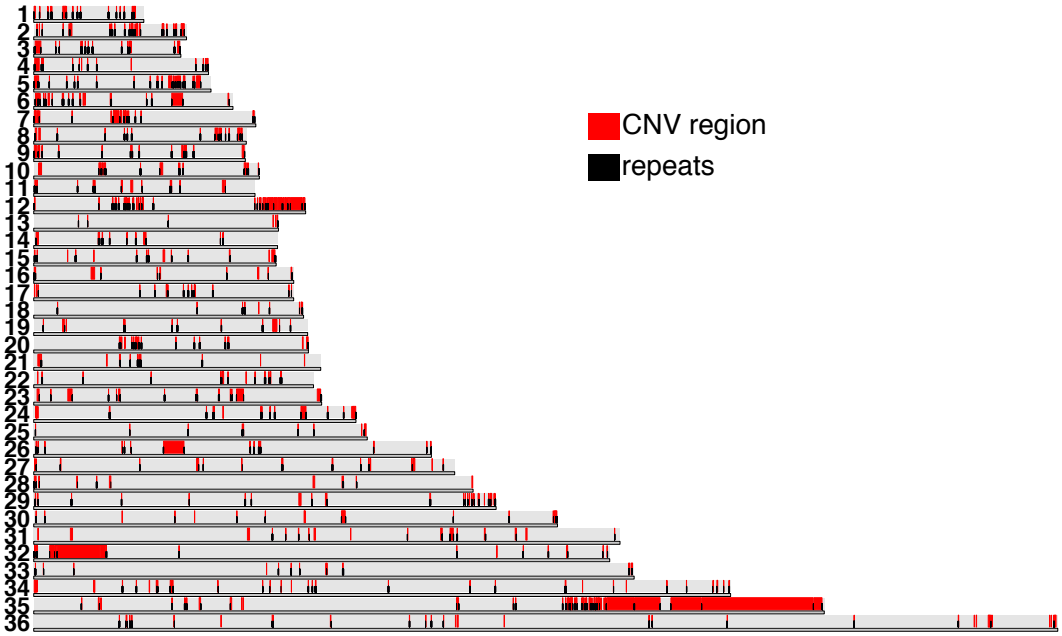

Genomic distribution of CNV regions and DNA sequence repeats. *Leishmania* chromosomes of the LdBPKv2 (*7*) are represented as stacked bars with karyoploteR (R package version 1.6.3) (*85*). The collapsed CNV sequence bins are shown in red. The repeat elements significantly associated with the CNV regions and mapping within their boundaries (1kb toward the outside and 150bp toward the inside of each collapsed CNV region) are shown in black.

818 **Fig. S2**

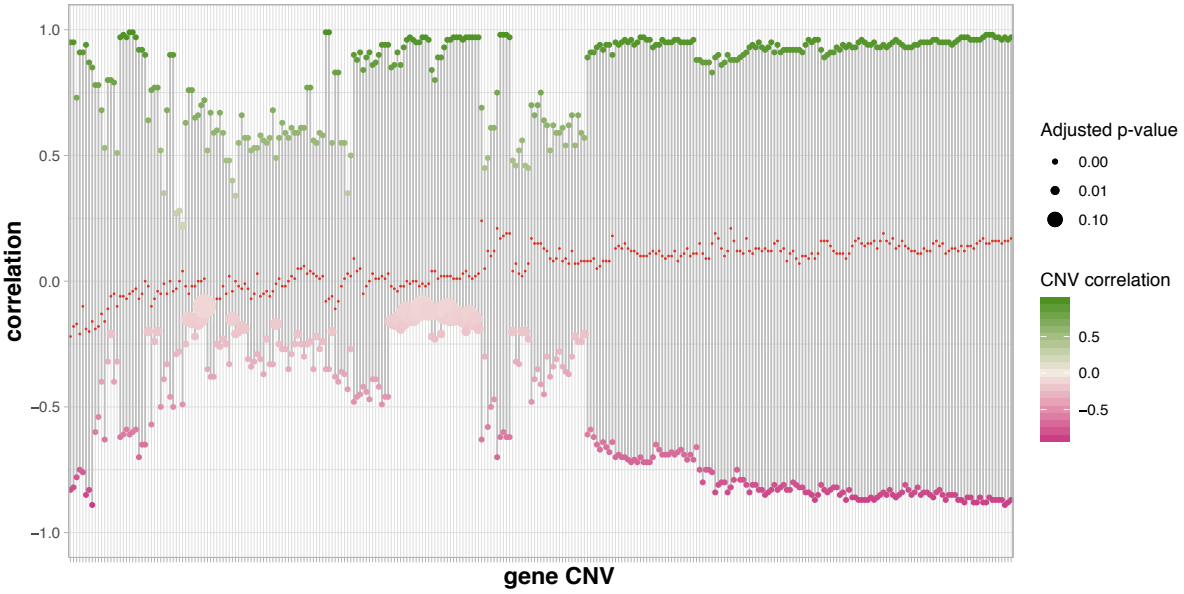

819

820 **Distribution of correlation values measured between gene CNVs pairs.** Each column indicates

821 a different gene CNV. The *y*-axis reports the Pearson correlation value of the most positively (top,

822 green) and most negatively (bottom, pink) correlated gene CNVs. The color intensity and the size

823 of the dots match respectively to the correlation and the adjusted p-value scores. The red notches

824 in the center indicate the median correlation scores.

825 **Fig. S3**

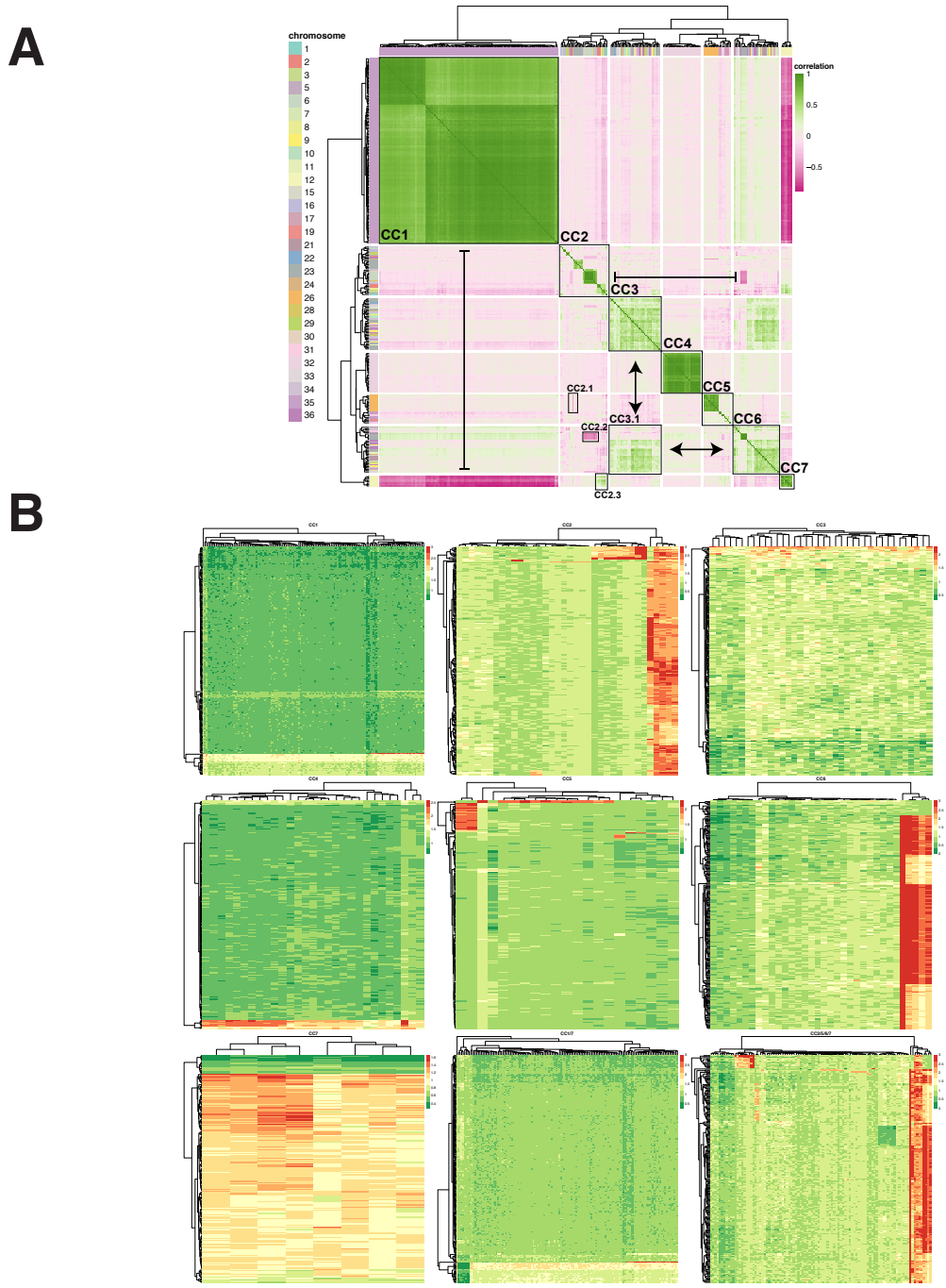

826

827 **All-vs-all gene CNV correlation.** (**A**) The heatmap shows gene CNVs on both axes. The color

828 range reflects the Pearson normalized coverage correlation value of gene CNVs across 204

829 samples. The side ribbon indicates the chromosomal localization of the gene CNV as defined in

830 the legend. Black boxes highlight correlations clusters (CC). The arrows indicate higher-level
831 interactions between clusters. Pointy and flat arrowheads indicate respectively correlation and anti-
832 correlation between clusters. (**B**) The heatmaps show the normalized coverage values of the gene
833 CNVs (columns) belonging to the correlation clusters defined in panel A with respect to the 204
834 samples (rows). Green and red indicate respectively low and high coverage values as indicated in
835 the legends. To ease the visualization, all scores of > 3 were assigned to a value of 3. The two last
836 heatmaps show a combination of multiple CCs. In CC1/7 the columns include both CC1 and CC7
837 gene CNVs. In CC2/5/6/7 the columns include CC2, CC5, CC6, CC7 gene CNVs.

838 **Fig. S4**

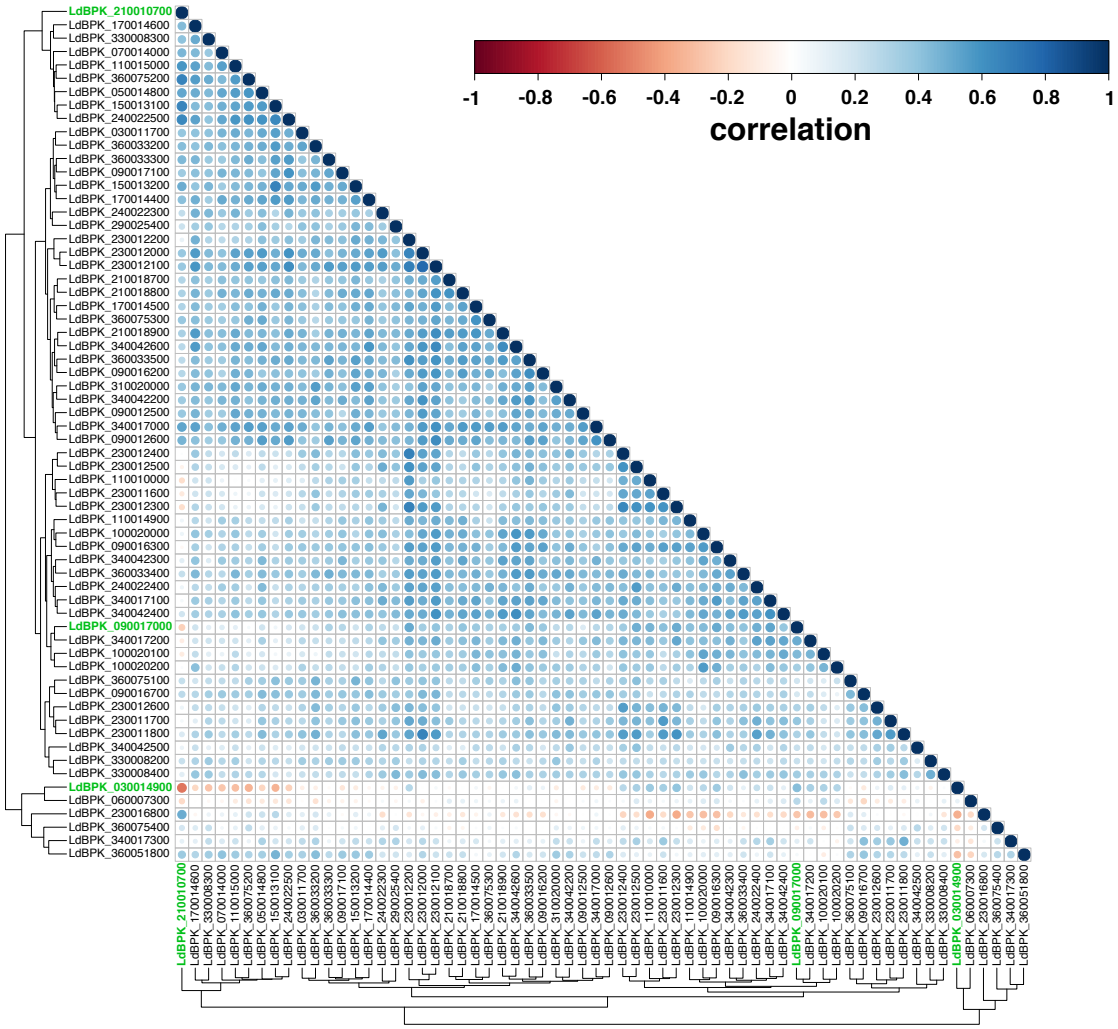

839

840 **tRNA gene CNV correlation map.** Both the *x*- and *y*-axes report gene CNVs. In green are labeled
841 three genes that are network-hubs as judged by their high connectivity (LdBPK_210010700,
842 rRNA; LdBPK_090017000, tRNA; LdBPK_030014900, eukaryotic translation initiation factor 2
843 subunit alpha). The color range of the dots reflects normalized coverage correlation value of the
844 gene CNVs. The level and direction of correlation are indicated by both dot size and color (red,
845 negative correlation; blue, positive correlation).

846 **Fig. S5**

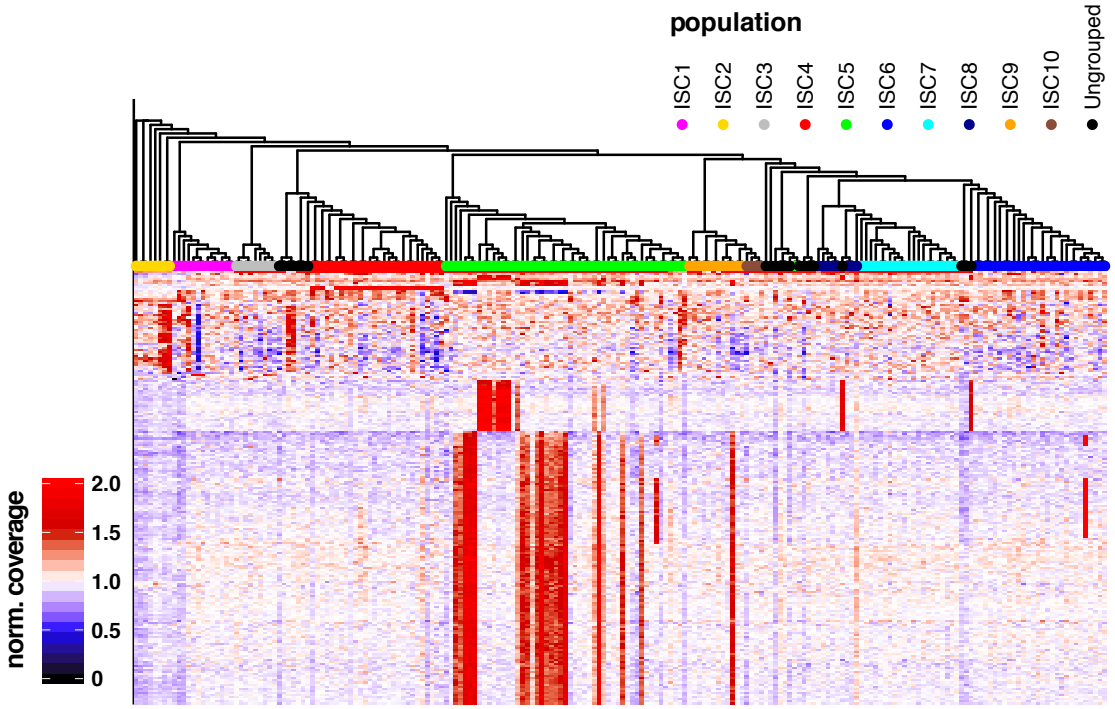

847

848 **Polyphyletic distribution of gene CNVs.** Cladogram based on SNVs (>90% frequency) (upper
849 panel) and heatmap (lower panel) generated for the 204 ISC isolates. The cladogram topology
850 demonstrates the relationships between isolates. The branch length does not reflect genetic
851 distance. The heatmap has the same layout as in **Fig. 1E**.

852 **Fig. S6**

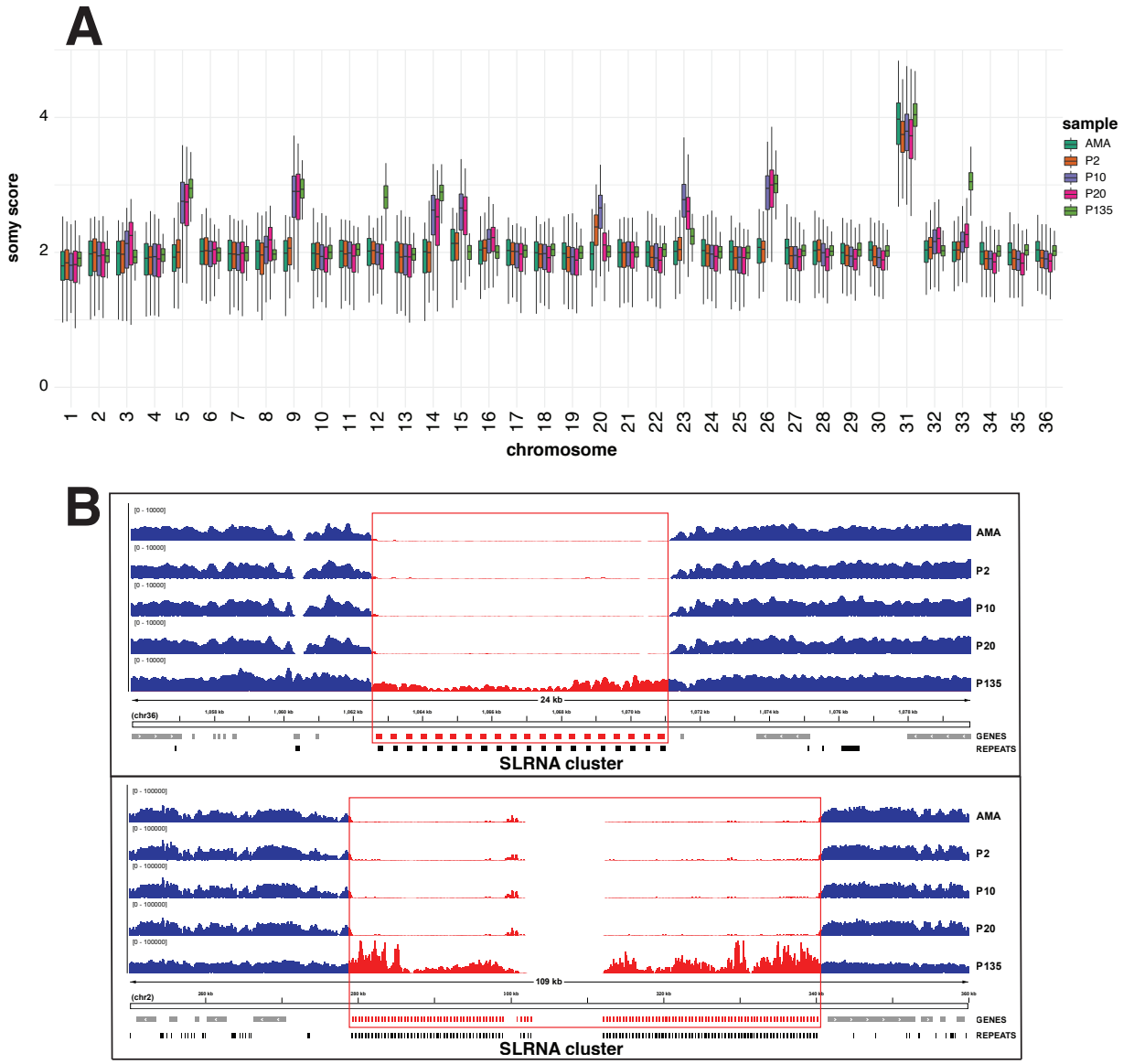

853

854 **Chromosome and gene copy number comparison of splenic amastigotes (AMA) and derived**

855 **promastigotes at different culture passages P2, 10, 20 and 135**. (**A**) The box plots demonstrate

856 the normalized sequencing coverage distributions of each chromosome. Bases where more than

857 50% of the reads have a MAPQ score lower than 50 were not considered. The somy score measured

858 on the *y*-axis is an estimation of the chromosome copy number (see methods). Chromosome 21

859 showed a steady disomic level across this sample set and thus was used to normalize the read depth

860 of the other chromosomes. (**B**) Examples of detected CNV gene clusters. Each panel illustrates a
861 genome browser representation of the sequencing depth measured in the samples (see methods).
862 Gene annotations and the predicted repetitive elements are indicated.

863 **Fig. S7**

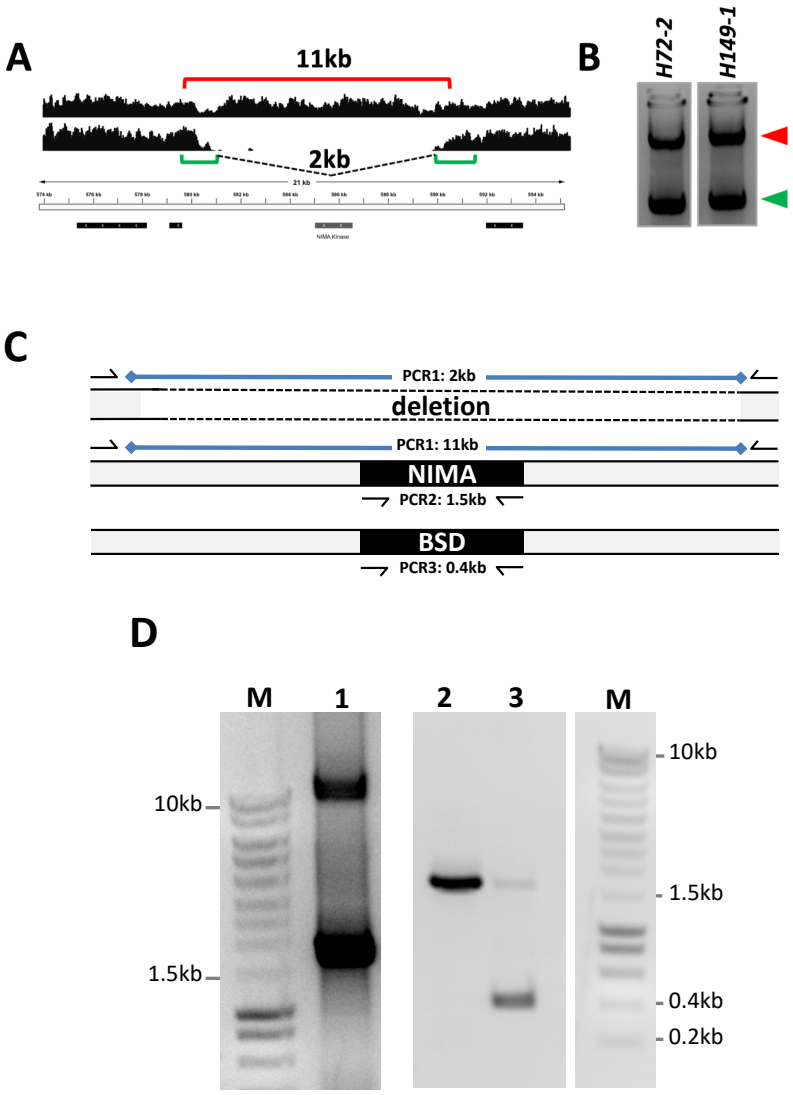

864

865 **Generation of heterozygous NIMA null mutants using CRISPR/Cas9 gene editing.** (**A**)
866 Schematic representation of the NIMA locus, indicating the 11kb and 2kb PCR fragments
867 diagnostic for the WT and deleted locus, respectively. (**B**) Gel electrophoretic separation of PCR
868 fragments obtained from two independent splenic isolates purified from hamsters. The arrows
869 heads indicate the 11kb (red) and 2kb (green) PCR fragments. (**C**) Schematic representation of the
870 PCR amplification strategy. Given the size of the genomic fragment under investigation and the
871 repetitive sequence surrounding the deletion site, a nested PCR protocol was applied first

872 amplifying the target locus (PCR1) before reamplification of the open reading frames for the
873 NIMA-related kinase gene (NIMA, PCR2) or the blasticidin resistance gene (BSD, PCR3). The
874 PCR primers are indicated by the arrows. (**D**) Gel electrophoretic separation of PCR fragments
875 obtained from a culture-adapted parasite population at *in vitro* passage 3 before gene editing using
876 primer pair for PCR1 (lane 1), and of a representative NIMA+/- heterozygous clone using primer
877 pairs PCR2 and PCR3 (lanes 2 and 3). The molecular weights of standard DNA marker fragments
878 (M) are indicated.

879 **Fig. S8**

gene identifier	annotation
Ld1S_070847100	paraflagellar rod protein, putative
Ld1S_080869200	intraflagellar transport protein 122B, putative
Ld1S_160120000	Flagellar calcium-binding protein, putative
Ld1S_160120100	flagellar calcium-binding protein, putative
Ld1S_160120200	flagellar calcium-binding protein, putative
Ld1S_160125800	paraflagellar rod protein 2C
Ld1S_160126200	paraflagellar rod protein 2C
Ld1S_160128500	Flagellar Member 3
Ld1S_270358700	Flagella connector protein 1
Ld1S_290432600	paraflagellar rod protein 1D, putative
Ld1S_290433000	paraflagellar rod protein 1D, putative
Ld1S_320533400	Flagellum attachment zone protein 9
Ld1S_320534400	dynein light chain, flagellar outer arm, putative
Ld1S_320535200	intraflagellar transport protein 140, putative
Ld1S_320549600	Paraflagellar Rod Proteome Component 9, putative
Ld1S_330583300_pseudogene	paraflagellar rod component, putative
Ld1S_330583400	intraflagellar transport protein 57,55, putative
Ld1S_330604900	Flagellum attachment zone protein 12
Ld1S_330611700	Flagellar Member 8 fragment
Ld1S_350689100	Flagellar Member 5
Ld1S_360750100	Flagellar Member 1
Ld1S_360766000	paraflagellar rod component, putative
Ld1S_360771700	paraflagellar rod component, putative
Ld1S_360783000	paraflagellar rod component, putative

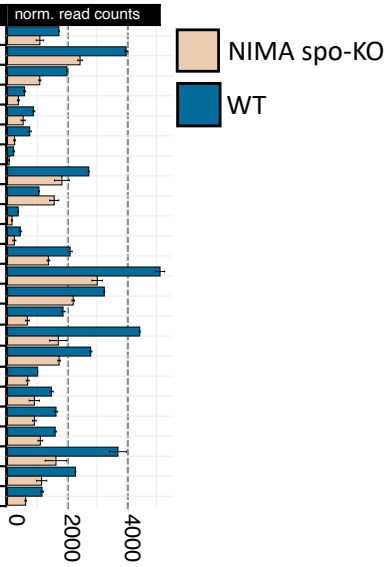

880

881 **Functional analysis of genes differentially expressed between spo-KO and WT clones.** Bar
882 plot (right panel) showing the normalized mean RNAseq read counts of the genes related to
883 flagellar function that were differentially expressed between WT (mean of two clones) and the six
884 NIMA-kinase spo-KO clones. For each entry, the gene identifier and the annotated function are
885 shown (left panel). The error bars indicate the standard deviations from the mean.

886

887 **Fig. S9**

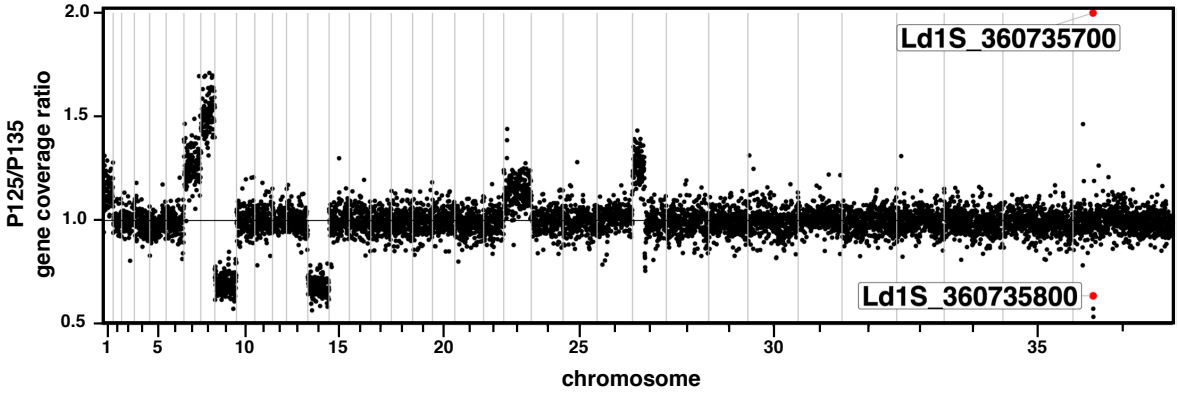

888
889

890 **Different parasite populations show distinct evolutionary trajectories.** (**A**) Genome-wide gene
891 coverage ratio between sample P125 and P135. Each dot represents a different gene. Vertical lines
892 mark chromosome boundaries. The deleted NIMA-kinase gene (Ld1S_360735700) and its
893 homologue (Ld1S_360735800) are indicated by the red dot. To ease plot readability, all scores of
894 > 2 were assigned to a value of 2.

895

896

897 **Fig. S10**

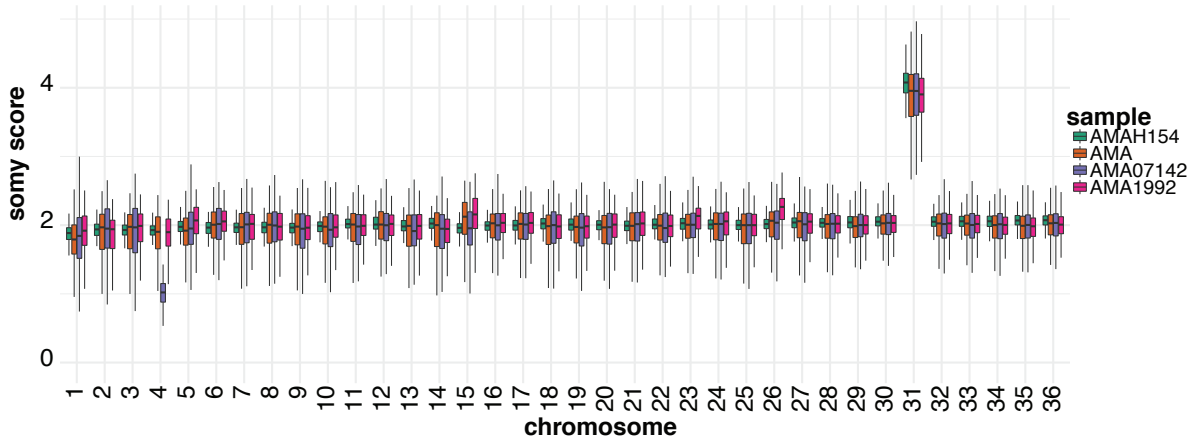

898

899 **Chromosome ploidy analysis.** The plot shows the karyotypic heterogeneity of four independent

900 amastigote isolates (AMAH154, AMA, AMA07142, AMA1992). Same layout as in **Fig. S6A**, but

901 the stable disomic chromosomes used for normalization was 25.

902

903 **Fig. S11**

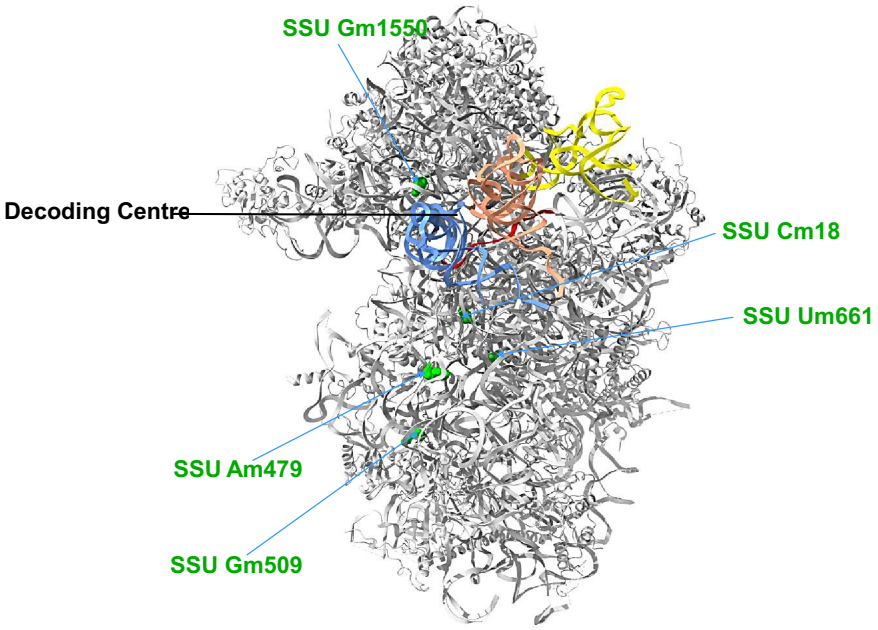

904

905 **3D-structure of the ribosome small subunit (SSU) depicting the hypermodified Nm sites.** The
906 hypermodified Nm sites are shown in green. The location of the decoding center is indicated. The
907 tRNAs positioned in the ribosome A (blue), P (orange) and E (yellow) sites are shown. The mRNA
908 being translated in the ribosome is indicated in red. The representation is based on the previously
909 deposited *L. donovani* ribosome SSU cryo-EM coordinates (Protein Data Bank (*39*) accession
910 6AZ1) (*40*).

911

912 **Data S1. (separate file)**
913 **Table S1: Mapping statistics of the dataset for the 204 clinical isolates.**

914 **Data S2. (separate file)**
915 **Table S2: Position and normalized coverage values of the collapsed CNV regions.**

916 *Footnote: The values reported for each sample indicate the normalized collapsed CNV coverage.*

917 **Data S3. (separate file)**
918 **Table S3: Repetitive elements.**

919 *Footnotes: The columns "GC%" and "N%" indicate respectively GC (guanine-cytosine) and the*
920 *undetermined bases content. The "longest ORF" column indicates the length of the amino acid*
921 *sequence of the longest open reading frame computed with EMBOSS getorf (version 6.6.0) (86)*
922 *with option "-find 1". (*) The observed count. (**) The expected count based on the sampled*
923 *CNV boundaries. (***) The value at the 5% percentile of random samples. (****) The value at*
924 *the 95% percentile of random samples. (*****) The standard deviation of random samples.*
925 *(******) The fold enrichment, given by the ratio observed / expected. (*******) Log2 of the fold*
926 *enrichment value. (********) The p-value of enrichment/depletion. (*********) The multiple-*
927 *testing corrected p-value.*

928 **Data S4. (separate file)**
929 **Table S4: Most positive and most negative LdBPK gene coverage correlations.**

930 **Data S5. (separate file)**
931 **Table S5: Correlation map data.**

932 *Footnote: The first three columns and the first three rows indicate respectively LdBPKv1 gene*
933 *identifiers, gene annotations and LdBPKv2 gene identifiers.*

934 **Data S6. (separate file)**
935 **Table S6: Correlation network data.**

936 *Footnote: The first three columns and the first three rows indicate respectively LdBPKv1 gene*
937 *identifiers, gene annotations and LdBPKv2 gene identifiers.*

938 **Data S7. (separate file)**
939 **Table S7: Network hub genes.**

940 **Data S8. (separate file)**
941 **Table S8: Collapsed CNVs showing highest read depth in the 204 *L. donovani* field isolates.**

942 *Footnote: (*) Maximum measured coverage of the top 30 collapsed CNV detected in genic areas.*

943 **Data S9. (separate file)**
944 **Table S9: Genes amplified in phylogenetically distinct clades.**

945 *Footnote: The values reported for each sample indicate the normalized gene coverage.*

946 **Data S10. (separate file)**
947 **Table S10: Normalized gene coverage values across ISC samples.**

948 *Footnote: The values reported for each sample indicate the normalized gene coverage.*

949 *(*) Difference between maximum and minimum normalized gene coverage.*

950 **Data S11. (separate file)**
951 **Table S11: Polysomy level analyses of two sets of Ld1S samples: (i) AMA to P135 isolates;**
952 **(ii) four AMA isolates.**

953 **Data S12. (separate file)**
954 **Table S12: Ld1S annotation.**

955 *Footnote: (*) Gene Ontology (GO) identifiers of the biological process (BP), molecular function*
956 *(MF) and cellular component (CC). (**) LdBPKv1 homologs predicted with OrthoFinder. Genes*
957 *with no significant match were searched with NCBI-blastn. One-to-many homologs are reported*
958 *with comma separated gene identifiers.*

959 **Data S13. (separate file)**
960 **Table S13: Definitions of gene clusters in two sets of Ld1S samples: (i) AMA-P135 isolates;**
961 **(ii) P20 clones isolates.**

962 **Data S14. (separate file)**
963 **Table S14: Gene CNVs and cluster CNVs detected during Ld1S culture adaptation.**
964 *Footnotes: (*) The AMA, P2, P10, P20 and P135 columns indicate the normalized gene coverage*
965 *in the respective samples. (**) "increasing" gene CNVs have a P135 normalized coverage*
966 *increase of at least 0.5 with respect to AMA. "decreasing" gene CNVs have a P135 normalized*
967 *coverage decrease of at least 0.5 with respect to AMA. All the other gene CNVs are labeled as*
968 *"transient". (***) The number of genes in the gene cluster (clstr). Individual (non-cluster) genes*
969 *have by default a value of 1. (****) Gene Ontology (GO) identifiers of the biological process (BP),*
970 *molecular function (MF) and cellular component (CC). (*****) The genes belonging to each*
971 *cluster CNV are reported as separate entries sharing the same attributes.*

972 **Data S15. (separate file)**
973 **Table S15: Gene CNVs and cluster CNVs detected in the eight Ld1S P20 clones.**
974 *Footnotes: (*) The CL1, CL3, CL4, CL6, CL7, CL8, CL9 and CL10 columns indicate the*
975 *normalized gene coverage in the respective samples. (**) The number of genes in the gene cluster*
976 *(clstr). Individual (non-cluster) genes have by default a value of 1. (***) Gene Ontology (GO)*
977 *identifiers of the biological process (BP), molecular function (MF) and cellular component (CC).*
978 *(****) The genes belonging to each cluster CNV are reported as separate entries sharing the same*
979 *attributes.*

980 **Data S16. (separate file)**
981 **Table S16: Single nucleotide variants (SNVs) in Ld1S P20 clones.**

982 *Footnotes: (*) Number of alternate observations, (**) Total read depth at the locus, (***)*
983 *Alternate allele quality sum in phred, (****) Reference allele quality sum in phred, (*****) Mean*
984 *mapping quality of observed alternate alleles, (******) Mean mapping quality of observed*
985 *reference alleles, (*******) Reference base and alternate allele, (********) context sequence of*
986 *the variant (+/- 5bp), (*********) SnpEff predicted variant effect.*
987

988 **Data S17. (separate file)**
989 **Table S17: Data of the differential expression analysis.**

990 *Footnotes: DESeq2 was utilized to test differential gene expression between the NIMA spo-KO*
991 *and the WT clones groups. Significant genes (adjusted p-value < 0.01) with a log2 fold change >*
992 *0.5 were considered "enriched" in the NIMA spo-KO group, while those with a log2 fold change*
993 *< -0.5 were considered "depleted" in the NIMA spo-KO group. Maxi-circle genes were not*
994 *considered in the analysis. (*) Mean of normalized counts, taken over all samples, (**) log2 fold*
995 *change between the groups, (***) standard error of the log2 fold change estimate, (****) Wald*
996 *statistic, (*****) Wald test p-value, (******) Benjamini-Hochberg adjusted p-value.*

997 **Data S18. (separate file)**
998 **Table S18: DNA and RNA double-ratio data.**

999 *Footnotes: (*) Whole genome sequencing (DNA) ratio: the mean read counts in spo-KO clones is*
1000 *divided by the mean DNA read counts in WT clones. Both the numerator and denominator are*
1001 *normalized by the average library size. (**) RNAseq (RNA) ratio: the mean read counts in spo-*
1002 *KO clones is divided by the mean RNA read counts in WT clones. Both the numerator and*
1003 *denominator are normalized by the average library size. (***) Double-ratio score: the ratio*
1004 *between the RNA ratio and the DNA ratio. (****) P-values of the double-ratio scores. (*****)*

1005 *Genes with double-ratio score p-value < 0.01 are considered "destabilized" or "stabilized" for*
1006 *double-ratio scores < or > 1, respectively. (******) Gene Ontology (GO) identifiers of the*
1007 *biological process (BP), molecular function (MF) and cellular component (CC).*

1008 **Data S19. (separate file)**
1009 **Table S19: P125/P135 gene coverage ratio values.**

1010 *Footnote: (*) The P125 and P135 columns indicate the gene coverage normalized by the median*
1011 *gene coverage in the respective samples.*

1012 **Data S20. (separate file)**
1013 **Table S20: The complete stoichiometry of Nm sites in *L. donovani* rRNA.**

1014 *Footnote: Data are shown as mean ± SEM (standard error of mean). The fold change (FC) of*
1015 *RMS of individual Nms is presented and the hypermodified sites showing FC > 2 are highlighted.*
1016 *Note that we have not identified all the snoRNAs guiding the existing Nm modification. (*) The*
1017 *rRNA unit (LSU, SSU or 5.8S) and the nucleotide carrying the Nm modification are reported.*

1018 **Data S21. (separate file)**
1019 **Table S21: The relative fold-change of Ψs in *L. donovani* rRNA between P135 and P2**
1020 **parasites.**
1021
1022 *Footnote: (*) Four independent replicates (R). Only sites with log2 fold change (FC) >1.3 in all*
1023 *replicates are considered as hypermodified sites and are highlighted in pink.*

1024
1025

1026 **References**

1027 1. E. Darmon, D. R. Leach, Bacterial genome instability. *Microbiol Mol Biol Rev* **78**, 1-39
1028 (2014).
1029 2. D. Hanahan, R. A. Weinberg, Hallmarks of cancer: the next generation. *Cell* **144**, 646-674
1030 (2011).
1031 3. D. Hughes, D. I. Andersson, Evolutionary consequences of drug resistance: shared
1032 principles across diverse targets and organisms. *Nat Rev Genet* **16**, 459-471 (2015).
1033 4. N. McGranahan, C. Swanton, Clonal Heterogeneity and Tumor Evolution: Past, Present,
1034 and the Future. *Cell* **168**, 613-628 (2017).
1035 5. C. E. Clayton, in *Curr. Opin. Microbiol.* (2016), vol. 32, pp. 46-51.
1036 6. S. Michaeli, Trans-splicing in trypanosomes: machinery and its impact on the parasite
1037 transcriptome. *Future Microbiol* **6**, 459-474 (2011).
1038 7. F. Dumetz *et al.*, in *MBio*. (2017), vol. 8.
1039 8. S. A. Iantorno *et al.*, Gene Expression in Leishmania Is Regulated Predominantly by Gene
1040 Dosage. *mBio* **8**, (2017).
1041 9. P. Leprohon *et al.*, in *Nucleic Acids Res.* (2009), vol. 37, pp. 1387-1399.
1042 10. P. Prieto Barja *et al.*, in *Nat Ecol Evol*. (2017), vol. 1, pp. 1961-1969.
1043 11. M. B. Rogers *et al.*, in *Genome Res.* (2011), vol. 21, pp. 2129-2142.
1044 12. H. Imamura *et al.*, in *Elife*. (2016), vol. 5.
1045 13. P. J. Hastings, J. R. Lupski, S. M. Rosenberg, G. Ira, Mechanisms of change in gene copy
1046 number. *Nat Rev Genet* **10**, 551-564 (2009).
1047 14. C. Waldron, F. Lacroute, Effect of growth rate on the amounts of ribosomal and transfer
1048 ribonucleic acids in yeast. *J Bacteriol* **122**, 855-865 (1975).
1049 15. V. Chikne *et al.*, Small nucleolar RNAs controlling rRNA processing in Trypanosoma
1050 brucei. *Nucleic Acids Res* **47**, 2609-2629 (2019).
1051 16. X. H. Liang, Q. Liu, M. J. Fournier, rRNA modifications in an intersubunit bridge of the
1052 ribosome strongly affect both ribosome biogenesis and activity. *Mol Cell* **28**, 965-977
1053 (2007).
1054 17. U. Birkedal *et al.*, Profiling of ribose methylations in RNA by high-throughput sequencing.
1055 *Angew Chem Int Ed Engl* **54**, 451-455 (2015).
1056 18. S. Schwartz *et al.*, Transcriptome-wide mapping reveals widespread dynamic-regulated
1057 pseudouridylation of ncRNA and mRNA. *Cell* **159**, 148-162 (2014).
1058 19. V. Chikne *et al.*, A pseudouridylation switch in rRNA is implicated in ribosome function
1059 during the life cycle of Trypanosoma brucei. *Sci Rep* **6**, 25296 (2016).
1060 20. M. Ackermann *et al.*, Self-destructive cooperation mediated by phenotypic noise. *Nature*
1061 **454**, 987-990 (2008).
1062 21. J. K. Graham, M. L. Smith, A. M. Simons, Experimental evolution of bet hedging under
1063 manipulated environmental uncertainty in Neurospora crassa. *Proc Biol Sci* **281**, (2014).
1064 22. I. M. Rouzine, A. D. Weinberger, L. S. Weinberger, An evolutionary role for HIV latency
1065 in enhancing viral transmission. *Cell* **160**, 1002-1012 (2015).
1066 23. M. K. Stewart, B. T. Cookson, Non-genetic diversity shapes infectious capacity and host
1067 resistance. *Trends Microbiol* **20**, 461-466 (2012).
1068 24. J. Seger, H. J. Brockmann. (Oxford, UK: Oxford University Press, 1987), vol. 4, pp. 182–
1069 211.
1070 25. A. H. Yona *et al.*, Chromosomal duplication is a transient evolutionary solution to stress.
1071 *Proc Natl Acad Sci U S A* **109**, 21010-21015 (2012).

1072 26. K. S. Rajan *et al.*, Pseudouridines on Trypanosoma brucei spliceosomal small nuclear
1073 RNAs and their implication for RNA and protein interactions. *Nucleic Acids Res* **47**, 7633-
1074 7647 (2019).
1075 27. K. S. Rajan, V. Chikne, K. Decker, H. Waldman Ben-Asher, S. Michaeli, Unique Aspects
1076 of rRNA Biogenesis in Trypanosomatids. *Trends Parasitol* **35**, 778-794 (2019).
1077 28. M. Penzo *et al.*, Human ribosomes from cells with reduced dyskerin levels are intrinsically
1078 altered in translation. *FASEB J* **29**, 3472-3482 (2015).
1079 29. C. Bellodi *et al.*, H/ACA small RNA dysfunctions in disease reveal key roles for noncoding
1080 RNA modifications in hematopoietic stem cell differentiation. *Cell Rep* **3**, 1493-1502
1081 (2013).
1082 30. F. Ariey *et al.*, A molecular marker of artemisinin-resistant Plasmodium falciparum
1083 malaria. *Nature* **505**, 50-55 (2014).
1084 31. J. B. Koenderink, R. A. Kavishe, S. R. Rijpma, F. G. Russel, The ABCs of multidrug
1085 resistance in malaria. *Trends Parasitol* **26**, 440-446 (2010).
1086 32. A. Selmecki, A. Forche, J. Berman, Aneuploidy and isochromosome formation in drug-
1087 resistant Candida albicans. *Science* **313**, 367-370 (2006).
1088 33. A. H. Melnyk, A. Wong, R. Kassen, The fitness costs of antibiotic resistance mutations.
1089 *Evol Appl* **8**, 273-283 (2015).
1090 34. A. Ashworth, C. J. Lord, J. S. Reis-Filho, Genetic interactions in cancer progression and
1091 treatment. *Cell* **145**, 30-38 (2011).
1092 35. J. van de Haar *et al.*, Identifying Epistasis in Cancer Genomes: A Delicate Affair. *Cell* **177**,
1093 1375-1383 (2019).
1094 36. C. Kim *et al.*, Chemoresistance Evolution in Triple-Negative Breast Cancer Delineated by
1095 Single-Cell Sequencing. *Cell* **173**, 879-893 e813 (2018).
1096 37. R. Leinonen, H. Sugawara, M. Shumway, I. N. S. D. Collaboration, in *Nucleic Acids Res.*
1097 (2011), vol. 39, pp. D19-21.
1098 38. B. Cuypers *et al.*, Integrated genomic and metabolomic profiling of ISC1, an emerging
1099 Leishmania donovani population in the Indian subcontinent. *Infect Genet Evol* **62**, 170-178
1100 (2018).
1101 39. H. M. Berman *et al.*, The Protein Data Bank. *Nucleic Acids Res* **28**, 235-242 (2000).
1102 40. M. Shalev-Benami *et al.*, Atomic resolution snapshot of Leishmania ribosome inhibition
1103 by the aminoglycoside paromomycin. *Nat Commun* **8**, 1589 (2017).
1104 41. G. Bussotti *et al.*, Leishmania Genome Dynamics during Environmental Adaptation
1105 Reveal Strain-Specific Differences in Gene Copy Number Variation, Karyotype
1106 Instability, and Telomeric Amplification. *MBio* **9**, (2018).
1107 42. W. Li, A. Godzik, in *Bioinformatics*. (2006), vol. 22, pp. 1658-1659.
1108 43. J. T. Robinson *et al.*, in *Nat. Biotechnol.* (2011), vol. 29, pp. 24-26.
1109 44. F. Ramírez *et al.*, in *Nucleic Acids Res.* (2016), vol. 44, pp. W160-165.
1110 45. *R Core Team*.
1111 46. T. Barrett *et al.*, BioProject and BioSample databases at NCBI: facilitating capture and
1112 organization of metadata. *Nucleic Acids Res* **40**, D57-63 (2012).
1113 47. S. Steinbiss *et al.*, Companion: a web server for annotation and analysis of parasite
1114 genomes. *Nucleic Acids Res* **44**, W29-34 (2016).
1115 48. C. Camacho *et al.*, in *BMC Bioinformatics*. (2009), vol. 10, pp. 421.
1116 49. M. Aslett *et al.*, TriTrypDB: a functional genomic resource for the Trypanosomatidae.
1117 *Nucleic Acids Res* **38**, D457-462 (2010).

1118 50. D. M. Emms, S. Kelly, OrthoFinder: phylogenetic orthology inference for comparative
1119 genomics. *Genome Biol* **20**, 238 (2019).
1120 51. B. Buchfink, C. Xie, D. H. Huson, Fast and sensitive protein alignment using DIAMOND.
1121 *Nat Methods* **12**, 59-60 (2015).
1122 52. S. R. Eddy, Accelerated Profile HMM Searches. *PLoS Comput Biol* **7**, e1002195 (2011).
1123 53. J. Huerta-Cepas *et al.*, in *Nucleic Acids Res.* (2016), vol. 44, pp. D286-293.
1124 54. C. Aurrecoechea *et al.*, EuPathDB: the eukaryotic pathogen genomics database resource.
1125 *Nucleic Acids Res* **45**, D581-D591 (2017).
1126 55. UniProt, in *Nucleic Acids Res.* (2012), vol. 40, pp. D71-75.
1127 56. E. Camon *et al.*, The Gene Ontology Annotation (GOA) Database: sharing knowledge in
1128 Uniprot with Gene Ontology. *Nucleic Acids Res* **32**, D262-266 (2004).
1129 57. A. Smit, Hubley, R & Green, P. (2013-2015).
1130 58. J. Jurka *et al.*, in *Cytogenet. Genome Res.* (2005), vol. 110, pp. 462-467.
1131 59. J. M. Flynn *et al.*, RepeatModeler2: automated genomic discovery of transposable element
1132 families. *bioRxiv [856591]*, (2019).
1133 60. T. L. Bailey *et al.*, MEME SUITE: tools for motif discovery and searching. *Nucleic Acids*
1134 *Res* **37**, W202-208 (2009).
1135 61. A. R. Quinlan, I. M. Hall, in *Bioinformatics*. (2010), vol. 26, pp. 841-842.
1136 62. S. Kurtz *et al.*, in *Genome Biol.* (2004), vol. 5, pp. R12.
1137 63. A. Heger, C. Webber, M. Goodson, C. P. Ponting, G. Lunter, GAT: a simulation framework
1138 for testing the association of genomic intervals. *Bioinformatics* **29**, 2046-2048 (2013).
1139 64. A. J. Enright, S. Van Dongen, C. A. Ouzounis, An efficient algorithm for large-scale
1140 detection of protein families. *Nucleic Acids Res* **30**, 1575-1584 (2002).
1141 65. G. C. a. T. Nepusz, The igraph software package for complex network research.
1142 *InterJournal* **Complex Systems**, 1695 (2006).
1143 66. T. M. J. R. Fruchterman, Edward M., Graph Drawing by Force-Directed Placement.
1144 *Software – Practice & Experience* **21**, 1129–1164 (1991).
1145 67. A. Stamatakis, RAxML version 8: a tool for phylogenetic analysis and post-analysis of
1146 large phylogenies. *Bioinformatics* **30**, 1312-1313 (2014).
1147 68. E. Garrison, G. Marth, in *arXiv preprint arXiv:1207.3907 [q-bio.GN]*. (2012).
1148 69. G. Yu, T. T. Lam, H. Zhu, Y. Guan, Two Methods for Mapping and Visualizing Associated
1149 Data on Phylogeny Using Ggtree. *Mol Biol Evol* **35**, 3041-3043 (2018).
1150 70. I. Letunic, P. Bork, Interactive Tree Of Life (iTOL) v4: recent updates and new
1151 developments. *Nucleic Acids Res* **47**, W256-W259 (2019).
1152 71. M. I. Love, W. Huber, S. Anders, Moderated estimation of fold change and dispersion for
1153 RNA-seq data with DESeq2. *Genome Biol* **15**, 550 (2014).
1154 72. S. Anders, P. T. Pyl, W. Huber, HTSeq--a Python framework to work with high-throughput
1155 sequencing data. *Bioinformatics* **31**, 166-169 (2015).
1156 73. P. Shannon *et al.*, Cytoscape: a software environment for integrated models of
1157 biomolecular interaction networks. *Genome Res* **13**, 2498-2504 (2003).
1158 74. S. Maere, K. Heymans, M. Kuiper, BiNGO: a Cytoscape plugin to assess
1159 overrepresentation of gene ontology categories in biological networks. *Bioinformatics* **21**,
1160 3448-3449 (2005).
1161 75. M. Ashburner *et al.*, Gene ontology: tool for the unification of biology. The Gene Ontology
1162 Consortium. *Nat Genet* **25**, 25-29 (2000).

1163 76. C. The Gene Ontology, The Gene Ontology Resource: 20 years and still GOing strong.
1164 *Nucleic Acids Res* **47**, D330-D338 (2019).
1165 77. P. Pescher, T. Blisnick, P. Bastin, G. F. Spath, Quantitative proteome profiling informs on
1166 phenotypic traits that adapt Leishmania donovani for axenic and intracellular proliferation.
1167 *Cell Microbiol* **13**, 978-991 (2011).
1168 78. T. Beneke *et al.*, A CRISPR Cas9 high-throughput genome editing toolkit for
1169 kinetoplastids. *R Soc Open Sci* **4**, 170095 (2017).
1170 79. S. M. Murta, T. J. Vickers, D. A. Scott, S. M. Beverley, Methylene tetrahydrofolate
1171 dehydrogenase/cyclohydrolase and the synthesis of 10-CHO-THF are essential in
1172 Leishmania major. *Mol Microbiol* **71**, 1386-1401 (2009).
1173 80. M. Dacher *et al.*, Probing druggability and biological function of essential proteins in
1174 Leishmania combining facilitated null mutant and plasmid shuffle analyses. *Mol Microbiol*
1175 **93**, 146-166 (2014).
1176 81. J. H. LeBowitz, Transfection experiments with Leishmania. *Methods Cell Biol* **45**, 65-78
1177 (1994).
1178 82. G. Schumann Burkard, P. Jutzi, I. Roditi, Genome-wide RNAi screens in bloodstream form
1179 trypanosomes identify drug transporters. *Mol Biochem Parasitol* **175**, 91-94 (2011).
1180 83. H. Nakayama *et al.*, Method for Direct Mass-Spectrometry-Based Identification of
1181 Monomethylated RNA Nucleoside Positional Isomers and Its Application to the Analysis
1182 of Leishmania rRNA. *Anal Chem* **91**, 15634-15643 (2019).
1183 84. D. Eliaz *et al.*, Genome-wide analysis of small nucleolar RNAs of Leishmania major
1184 reveals a rich repertoire of RNAs involved in modification and processing of rRNA. *RNA*
1185 *Biol* **12**, 1222-1255 (2015).
1186 85. B. Gel, E. Serra, karyoploteR: an R/Bioconductor package to plot customizable genomes
1187 displaying arbitrary data. *Bioinformatics* **33**, 3088-3090 (2017).
1188 86. P. Rice, I. Longden, A. Bleasby, EMBOSS: the European Molecular Biology Open
1189 Software Suite. *Trends Genet* **16**, 276-277 (2000).
1190